Sustainable Cities and Society 118 (2025) 106019

Contents lists available at ScienceDirect

Sustainable Cities and Society

journal homepage: www.elsevier.com/locate/scs

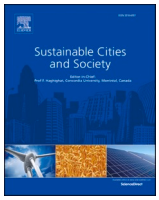

Observed determinants of urban outdoor thermal exposure during hot summer and snowy winter periods in a humid continental climate

Timothy Aiello [a], E. Scott Krayenhoff [a,*], Ariane Middel [b,c], Jon Warland [a]

[a] School of Environmental Sciences, University of Guelph, Guelph, Canada
[b] School of Arts, Media and Engineering, Arizona State University, Tempe, USA
[c] School of Computing and Augmented Intelligence, Arizona State University, Tempe, USA

ARTICLE INFO

Keywords:
Climate adaptation
Heat and cold stress
Mean radiant temperature
Microclimate
Pedestrian thermal comfort
Urban design

ABSTRACT

Many cities in the midlatitudes experience both extreme heat and cold, and pedestrians are exposed to thermal extremes that cause bodily stress. With growing urban populations, city design that contributes to mitigating summer heat while reducing winter cold exposure is increasingly important. Pedestrian thermal exposure depends on several microclimatic factors, including shortwave and longwave radiation absorption, which can be quantified by the mean radiant temperature (T_{mrt}). Limited research has been conducted on the radiative components of thermal exposure in hot, humid summers and cold, snowy winters. We gathered micrometeorological data from diverse urban sites and in multiple seasons in Guelph, Canada, using a mobile human-biometeorological weather station (*MaRTy* cart) that applies the six-directional method to determine T_{mrt}. Seasonal datasets were analysed and compared to examine the drivers of thermal exposure and recommend strategies for mitigating heat and cold stress. In summer, shade is the primary factor that reduces daytime heat exposure and it slightly increases nighttime heat exposure. Enhanced pervious ground cover is a secondary factor day and night. In winter, reduced shade alleviated daytime cold exposure, while snow cover provided daytime benefits from increased solar reflections and post-sunset penalties associated with reduced longwave radiation from low snow surface temperatures.

1. Introduction

Extreme heat is projected to increase in frequency, duration, and intensity as Earth's climate warms (IPCC, 2021, 2014). Moreover, urban growth, which usually entails the replacement of greenery with impervious surfaces, contributes to additional warming. Expanding and densifying cities are associated with reduced transpiration by vegetation and increasing surface area of materials that effectively absorb, retain, and release heat. Impervious surfaces contribute to higher daytime surface temperatures and elevate surface and air temperatures during evening and nighttime (Argueso et al., 2014; Krayenhoff et al., 2018; Stewart et al., 2021). By 2050, urban populations are expected to increase substantially, with the majority of growth occurring in Africa and Asia (United Nations, 2019). In Canada, more than 70 % of residents live in urbanized areas, with this percentage expected to increase (Statistics Canada, 2021). Furthermore, shifting Canadian demographics will result in disproportionate levels of older residents, who will be more sensitive and vulnerable to extreme heat from climate change and urbanization (Di Matteo, 2005; Government of Canada, 2019).

Exposure to extreme heat can lead to increased human morbidity and mortality (Gosling et al., 2009; Hondula et al., 2015), especially in growing urban areas (Wouters et al., 2017). However, research has found that there is greater morbidity and mortality in winter than in the summer (McGeehin & Mirabelli, 2001; Analitis et al., 2008), which is relevant to a city such as Guelph, Ontario, where seven months of the year have a daily air temperature average below 10 °C. The relationship between morbidity/mortality and air temperature is U-shaped, with increased health impacts at high and low temperatures. However, mortality attributed to cold exposure has a greater temporal lag than that attributed to heat exposure (Chen et al., 2016). Thus, increased rates of illness associated with low ambient air temperatures occur days or weeks after exposure, especially after prolonged cold spells (Chen et al., 2016). While the studies mentioned above associate health impacts with air temperature, actual thermal exposure or stress of individuals depends on several factors in addition to air temperature.

The term "thermal exposure" is used here to indicate the meteorological components of thermal comfort (which also includes

* Corresponding author.
E-mail address: skrayenh@uoguelph.ca (E.S. Krayenhoff).

https://doi.org/10.1016/j.scs.2024.106019
Received 10 August 2024; Received in revised form 24 October 2024; Accepted 26 November 2024
Available online 2 December 2024

List of Symbols

a_k	Absorption coefficient for shortwave radiation
a_l	Absorption coefficient for longwave radiation
σ	Stephan-Boltzmann constant, 5.67 $\times 10^{-8}$ W m^{-2} K^{-4}
K_i	Incident shortwave radiation from direction i, W m^{-2}
L_i	Incident longwave radiation from direction i, W m^{-2}
RH	Relative humidity, %
PET	Physiologically Equivalent Temperature, °C
T_a	Air temperature, °C
T_{mrt}	Mean radiant temperature, °C
T_{sfc}	Surface temperature, °C
$UTCI$	Universal Thermal Climate Index, °C
v	Wind speed, m s^{-1}
W_i	Angular weighting for a standing reference pedestrian incident from direction i
Ψ_{sky}	Upwards sky view factor
I_{360}	Lateral impervious view factor (buildings + ground-level impervious)
P_{360}	Lateral pervious view factor (tree + grass)
Sn_{360}	Lateral snow view factor

physiological, behavioural, and psychological factors). In contrast, "thermal stress" includes some physiological and behavioural factors in addition to thermal exposure. Therefore, thermal exposure is a component of thermal stress, which is, in turn, a component of thermal comfort (Guzman-Echavarria et al., 2023). In summer, thermal exposure to heat results from the combination of local surface and air temperature, wind speed, humidity, and shade availability. In winter, thermal exposure can lead to cold stress and is driven by the same meteorological factors. Differences in the relative and absolute importance of these factors occur between seasons (e.g., wind and shade decrease heat exposure during summer but increase cold exposure in winter; Givoni et al., 2003). In the context of the projected increases in extreme heat episodes, it is advantageous to consider modification of several of these variables in addition to commonly targeted factors such as air temperature and shade. An opinion survey in Wuhan, China, a humid sub-tropical climate similar to New York City, found that thermal comfort outranked other factors contributing to the quality of outdoor spaces, including air quality, the acoustic environment, convenience, and functionality (Lai et al., 2014). Similar prioritization of environmental conditions was found in an urban district in Italy (Piselli et al. 2018). To complement subjective studies of thermal comfort, it is important to quantify all meteorological factors that influence outdoor thermal comfort: solar and thermal radiation, humidity, wind speed, and air temperature.

Human biometeorology, the study of the interactions between people and the atmosphere, is a growing field, especially in urban environments (Hondula et al., 2017). Urban thermal exposure research has typically focused on summer, especially in hot, dry locations, and has recently begun to focus on explicit three-dimensional measurement of radiative effects (Ali-Toudert et al., 2005; Middel et al., 2020; Middel & Krayenhoff, 2019). Conversely, the relative environmental contributions to summer discomfort and associated optimal design strategies may differ between dry and humid cities. For example, recommendations from a study in Tempe, Arizona (Middel & Krayenhoff, 2019) may not be relevant in Guelph, Ontario, which is situated in a different climate zone. Studies should be conducted in cities in various climate zones to make climatically relevant recommendations.

Other studies that have assessed the contributions of the three-dimensional radiative environment to urban thermal exposure in relatively humid locations using the six-directional method (consisting of six pyranometers and six pyrgeometers oriented to capture radiation incident from above, below, and the four cardinal directions) have been limited to summertime measurements (Ali-Toudert & Mayer, 2007; Du et al., 2020a; Holst & Mayer, 2011; Kántor et al., 2018, 2016; Mayer et al., 2008). A study in Harbin, China (Du et al., 2020b) is the only one examining winter cold exposure. However, the impacts of snow on thermal exposure were minimally studied. Fresh snow has a high albedo, potentially increasing reflected shortwave radiation to pedestrians. The surface temperature of snow can also fall well below air temperature, limiting the amount of longwave radiation emitted compared to other surfaces (Oke et al., 2017).

The mean radiant temperature (T_{mrt}) is a crucial determinant of thermal exposure for many conditions and is often a major cause of microscale variability in thermal exposure. T_{mrt} is the "uniform temperature of an imaginary enclosure in which the radiant heat transfer from the human body equals the radiant heat transfer in the actual non-uniform enclosure" (ISO, 1998). It can be understood as the effective temperature felt by a body considering the impact of radiation emitted and reflected from surrounding surfaces, in addition to sky-derived shortwave and longwave irradiance. T_{mrt} is a component of several thermal stress indices, such as the Physiologically Equivalent Temperature (*PET*) (Höppe, 1999) and the Universal Thermal Climate Index (*UTCI*) (Jendritzky et al., 2012). Indices such as *PET* and *UTCI* combine micrometeorological conditions for a particular location with assumptions related to individual physiology and clothing to quantify the net thermal stress a "typical" pedestrian would experience.

Unlike a globe thermometer (Thorsson et al. 2007; Vanos et al. 2021), the six-directional method for measurement of T_{mrt} permits directional attribution of radiative heat incident on the pedestrian. This approach enables better quantification of how individual or groupings of urban facets impact thermal exposure, a critical step in designing comfortable spaces. Many studies have observed and modeled the impacts of urban design elements on three-dimensional radiation fluxes (Ali-Toudert & Mayer, 2007; Du et al., 2020a; Holst & Mayer, 2011; Kántor et al., 2018, 2016; Lai et al., 2018; Middel et al., 2021; Middel et al. 2023; Middel & Krayenhoff, 2019). For the first time, Middel and Krayenhoff (2019) decomposed six-directional T_{mrt} measurements in an extreme heat area while isolating the radiative contributions from the sky, vegetation, and impervious surfaces. T_{mrt} was also decomposed into its constituents for a wintertime case by Du et al. (2020b). Du et al. (2020b) measured six-directional radiation fluxes and other micrometeorological variables of relevance to thermal exposure at six urban locations during winter, with sky view factors (Ψ_{sky}) ranging from 0.333 to 0.763, and with snow either present at or adjacent to each site. Only building-induced shade was considered since the sites did not include trees. Observation at a more diverse collection of sites with a larger range of Ψ_{sky} values and a greater range of visible snow amounts should be considered to extend cold-climate wintertime measurements.

This project extends research by Middel and Krayenhoff (2019), using a human-biometeorological weather station (*MaRTy*) in a mid-latitude city with a large seasonal variation in climate. It also advances initial research by Du et al. (2020b) by examining a larger set of measurement sites in a cold climate and emphasizing the radiative impacts of snow. Ultimately, these measurements provide insights that may assist with the minimization of extreme outdoor thermal exposures in urban areas. While wintertime thermal exposures are often linked to wind and air temperature (Yao et al. 2018), recent evidence suggests that the radiative environment, which *MaRTy* is ideally suited to assess, can frequently be the most important factor (Xiong & He, 2022; Xu et al. 2018).

This study aims to measure all micrometeorological variables that influence human thermal exposure (relative humidity [RH], wind speed [v], air temperature [T_a], shortwave radiation [K], and longwave radiation [L]) in an urban area situated in a humid continental climate during clear sky conditions in three seasons. Collected micrometeorological data will contribute to the growing literature on urban thermal exposure measurements, especially those that apply the 6-directional method (e.g., with *MaRTy*), with the potential to inform urban

Sensor	Variable(s)	Range	Accuracy	Response Time	Height
HygroVUE10 T/RH Probe	Temperature	-40°C to +70°C	± 0.2°C	> 130 seconds	1.6 m
	Humidity	0% to 100%	± 1.5%	8 seconds	
R.M Young 3101 Wind Sentry Cup Anemometer	Wind Speed	0 to 50m s^{-1}	± 0.5 m s^{-1}	*** see note below**	1.8 m
Type T Thermocouple	Temperature	-45°C to +75°C	± 0.5°C	< 1 second	1.5 m
Garmin GPS16X GPS	Location	-	< 3m	< 2 seconds	1.45 m
Kipp & Zonen CNR4 Net Radiometers (3)	K_i Flux	0 to 2000 W m^{-2}	< 5%	< 18 seconds	1.3 m to 1.4 m
	L_i Flux	-250 to 250 W m^{-2} (net)	< 10%	< 18 seconds	

*** Wind Sentry cup anemometer has a measurement threshold of 0.5 m s^{-1}, independent of response time**

Fig. 1. The mobile human-biometeorological platform (*MaRTy* cart) designed to gather pedestrian thermal exposure data in Guelph, Canada during summer and winter (left). Sensors used on *MaRTy* for each variable, associated specifications, and the height each sensor is mounted (right).

planning and provide valuable data for evaluation of numerical models (e.g., Lachapelle et al. 2022; Jiang et al. 2023). The specific objectives of this study are:

1. Collect high-resolution micrometeorological data relevant to urban outdoor thermal exposure in a humid continental climate, including directional radiation flux data, using a mobile human-biometeorological station (*MaRTy*).
2. Aggregate measured data into thermal stress indices to assess and compare the spatio-temporal variation of pedestrian thermal exposure in hot humid and cold snowy weather.
3. Determine and recommend facets of urban design that minimize pedestrian exposure to excess heat and cold in multiple seasons and during both day and night.

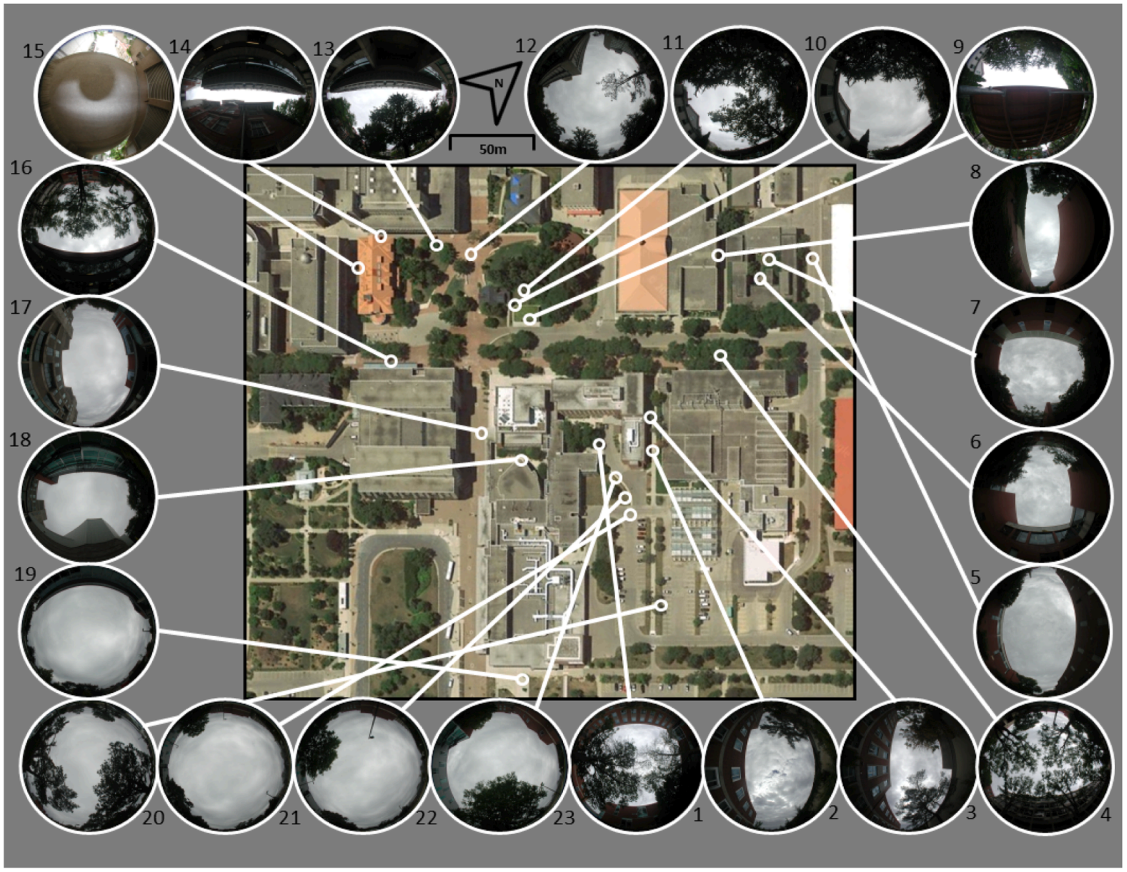

Fig. 2. Measurement sites on the University of Guelph campus as captured with an upwards-facing fisheye lens on a cloudy day (September 20, 2020).

Table 1
Summary of measurement site metadata and average *MaRTy* cart data observations for: the duration of measurements (12:00 to 22:00 EDT; mid-afternoon (15:00 EDT); and post-sunset (22:00 EDT) on June 6th, 2021.

							12:00 EDT - 22:00 EDT average							Solar maximum (15:00 EDT)							Night (22:00 EDT)						
ID	Surface Type	Shade Type	SVF	Lateral impervious view	Lateral pervious view	Sun hours	Tmrt [°C]	Tair [°C]	Tsfc [°C]	RH [%]	v [m/s]	PET [°C]	UTCI [°C]	Tmrt [°C]	Tair [°C]	Tsfc [°C]	RH [%]	v [m/s]	PET [°C]	UTCI [°C]	Tmrt [°C]	Tair [°C]	Tsfc [°C]	RH [%]	v [m/s]	PET [°C]	UTCI [°C]
1	Concrete	Tree/building quad	0.33	0.55	0.32	0.5	42.0	28.3	37.4	43.0	0.1	34.5	30.3	58.7	31.7	45.6	39.0	0.1	48.4	38.3	23.5	24.6	29.1	47.7	0.0	24.9	24.0
2	Concrete	NE/SW canyon	0.50	0.58	0.20	7.0	37.2	28.2	33.7	43.5	0.7	30.9	29.3	54.0	31.6	37.9	41.0	0.7	42.1	37.2	21.6	24.6	25.9	48.0	0.0	23.8	23.4
3	Concrete	Tree NE/SW canyon	0.27	0.59	0.29	4.7	36.8	28.2	28.9	43.6	0.2	29.7	28.4	39.2	31.6	31.2	40.9	0.1	36.3	33.5	23.2	24.6	25.1	48.2	0.0	24.9	23.9
4	Brick	Trees/ SE building	0.19	0.54	0.31	5.7	37.7	27.9	27.2	43.9	0.3	30.6	28.6	43.3	30.7	30.5	41.8	0.0	39.0	33.8	23.2	24.6	23.2	48.0	0.0	24.8	23.8
5	Asphalt	NE/SW canyon	0.57	0.59	0.12	7.0	40.2	28.1	36.6	42.9	0.6	34.4	30.4	63.8	31.0	44.6	40.0	0.0	49.3	38.4	22.9	24.6	26.7	47.6	0.0	24.7	23.8
6	Asphalt	brick quadrangle	0.41	0.68	0.16	6.2	40.1	28.2	30.5	44.1	0.1	33.0	29.6	50.7	31.3	34.3	41.2	0.0	43.7	36.2	23.4	24.6	25.0	48.6	0.0	25.0	24.0
7	Grass	brick quadrangle	0.49	0.26	0.53	8.5	37.6	28.1	27.6	43.7	0.5	31.1	29.1	54.8	31.4	32.9	41.2	1.1	42.7	37.0	20.5	24.6	20.4	48.4	0.0	23.3	23.1
8	Asphalt	NE/SW canyon	0.28	0.53	0.34	3.5	37.4	28.2	35.7	43.6	0.2	29.9	28.7	39.5	31.4	38.1	40.9	0.1	35.8	33.4	24.5	24.6	27.5	48.1	0.1	25.1	24.3
9	Concrete	Green Roof	0.13	0.66	0.27	0.2	33.4	27.9	25.1	43.6	0.5	29.4	28.3	40.2	31.1	25.8	40.9	0.7	34.6	33.2	23.2	24.5	24.1	48.3	0.0	24.9	23.9
10	Grass	Tree	0.40	0.25	0.54	7.3	32.9	27.9	28.1	43.8	0.5	31.4	28.7	51.8	31.1	35	41.7	0.5	44.3	36.3	20.1	24.5	18.2	48.2	0.0	23.1	22.9
11	Grass	Trees	0.19	0.13	0.77	5.8	32.2	27.9	26.1	43.7	0.3	30.6	28.7	50.3	31.1	33.8	41.4	0.0	41.5	35.9	21.0	24.4	18.8	48.4	0.0	23.3	23.1
12	Brick	Tree	0.54	0.60	0.12	9.8	37.6	27.9	36.2	43.3	1.0	29.8	28.7	56.1	31.2	46.9	40.7	1.5	39.7	36.0	20.8	24.4	24.0	48.4	0.0	23.3	23.1
13	Brick	NW/SE building/tree	0.14	0.72	0.19	6.3	38.2	27.9	27.3	43.9	0.6	31.0	28.6	46.5	31.2	34.7	42.2	0.0	41.4	35.1	24.0	24.4	23.3	48.6	0.0	25.2	24.0
14	Asphalt	NW/SE canyon	0.11	0.92	0.03	3.8	35.4	28.0	26.8	43.1	1.1	29.5	28.3	46.3	31.3	33	41.0	2.6	37.3	34.3	25.0	24.5	23.9	48.0	0.2	25.1	24.3
15	Concrete	Tunnel	0.03	0.98	0.01	0.0	34.2	28.0	22.4	43.0	0.7	26.7	26.9	27.1	31.1	22.1	41.0	1.0	29.2	29.8	24.8	24.7	22.7	47.7	0.2	25.0	24.5
16	Brick	NW/SE tree/glass	0.28	0.64	0.24	8.7	37.3	28.1	31.6	43.1	0.1	32.3	29.3	51.4	31.2	37.9	39.8	0.0	44.3	36.2	22.9	24.8	23.5	47.1	0.0	24.7	23.9
17	Brick	NE/SW canyon	0.49	0.73	0.00	6.5	38.5	28.3	39.0	42.7	0.3	31.4	29.2	44.5	31.5	49.4	39.8	0.1	38.8	34.7	23.4	24.8	27.6	46.8	0.0	25.1	24.0
18	Concrete	NW/SE canyon	0.41	0.70	0.10	9.3	43.1	28.4	31.6	42.4	0.3	32.8	30.4	63.8	31.8	41.5	39.2	1.2	45.6	39.3	22.7	24.8	26.8	46.9	0.0	24.7	23.9
19	Concrete	-	0.79	0.53	0.06	11.8	40.9	28.3	37.1	43.0	1.7	32.0	29.8	68.4	31.4	46.9	40.9	1.3	47.4	40.2	20.2	24.9	26.8	47.1	0.7	21.3	22.9
20	Concrete	Tree	0.42	0.30	0.47	6.3	39.6	28.3	38.0	42.5	2.3	28.7	27.9	53.2	31.6	47.1	39.5	1.2	37.9	34.6	21.0	24.8	27.4	47.1	1.1	21.0	22.7
21	Asphalt	-	0.80	0.48	0.10	12.0	41.9	28.3	41.7	42.6	0.7	32.3	30.3	62.3	31.6	53.5	39.4	1.9	43.3	38.1	20.5	24.8	28.5	47.1	0.0	23.4	23.1
22	Grass	-	0.73	0.17	0.48	10.2	38.4	28.4	26.1	42.8	1.1	31.5	29.8	59.5	31.8	32.8	40.0	1.4	43.1	38.1	17.7	24.7	15.3	47.3	0.0	21.8	22.3
23	Grass	Tree	0.57	0.16	0.54	10.0	35.2	28.4	22.7	42.5	0.5	31.2	29.5	56.6	31.9	29.1	38.4	1.2	42.1	37.6	18.9	24.7	16.6	47.5	0.0	22.5	22.6

Legend: Highest | 2nd Highest | 3rd Highest | Lowest

Table 2
Summary of measurement site metadata and forecasted *MaRTy* cart observations for: the total day (11:00 EST to 18:30 EST); solar maximum (12:00 EST); and post-sunset on February 3rd, 2021.

							11:00 EST - 18:30 EST average						Solar maximum (12:00 EST)						Night (18:30 EST)					
ID	Surface Type	Shade Type	SVF	Lateral impevious view	Lateral snow view	Sun Hours	Tmrt [C]	Tair [C]	Tsfc [C]	RH [%]	v [m/s]	UTCI [C]	Tmrt [C]	Tair [C]	Tsfc [C]	RH [%]	v [m/s]	UTCI [C]	Tmrt [C]	Tair [C]	Tsfc [C]	RH [%]	v [m/s]	UTCI [C]
1	Snow/concrete	Tree/building quad	0.54	0.74	0.25	1.3	3.2	-1.6	-5.6	54.1	0.7	-1.0	17.3	-1.6	-5.4	50.1	0.4	6.262	-9.8	-3.2	-7.5	60.3	0.9	-6.0
2	Concrete	NE/SW canyon	0.45	0.73	0.15	3.8	-0.7	-1.7	-5.9	54.3	1.5	-5.6	7.5	-1.8	-5.4	50.4	1.3	-3.82	-9.4	-3.2	-7.3	60.3	2.0	-9.9
3	Concrete	Tree NE/SW canyon	0.42	0.77	0.12	1.8	-1.6	-1.9	-5.1	54.6	2.1	-9.8	3.6	-2.1	-5.4	51.0	1.7	-6.26	-7.6	-3.2	-5.5	60.2	1.8	-10.0
4	Brick	Trees/ SE building	0.53	0.65	0.10	0.2	5.0	-2.1	-5.1	55.1	0.7	0.5	-0.6	-2.3	-6.4	51.5	0.2	-1.09	-8.5	-3.3	-6.4	60.6	1.0	-6.1
5	Asphalt	NE/SW canyon	0.57	0.73	0.05	1.8	11.3	-2.0	-6.0	56.4	1.9	-3.7	38.9	-2.2	-5.3	53.6	1.5	9.436	-7.7	-3.2	-7.3	61.3	1.8	-10.4
8	Asphalt	NE/SW canyon	0.30	0.78	0.11	1.7	-2.8	-1.9	-1.5	55.3	1.8	-8.7	-0.1	-2.2	-1.2	51.8	2.7	-13	-6.6	-3.2	-2.5	60.3	1.0	-7.1
9	Snow/concrete	Green Roof	0.23	0.80	0.40	0.2	1.2	-1.7	-3.5	55.3	0.1	0.1	4.1	-1.9	-3.8	52.0	0.2	1.001	-8.5	-3.2	-3.9	60.8	0.0	-4.5
10	Snow	Tree	0.41	0.67	0.46	3.8	10.0	-1.7	-6.9	55.3	0.2	3.4	38.9	-1.8	-6.3	51.9	0.2	14.85	-8.5	-3.2	-7.9	61.1	0.0	-4.5
11	Snow	Trees	0.41	0.60	0.45	5.8	15.8	-1.6	-2.9	54.8	0.3	5.2	46.8	-1.7	-1.6	51.1	0.0	18.04	-9.3	-3.1	-3.4	60.4	0.5	-6.9
12	Brick	Tree	0.59	0.64	0.03	5.0	19.1	-1.6	-3.5	54.2	1.7	0.6	43.8	-1.7	-2.4	50.0	1.8	7.97	-5.5	-3.1	-6.4	60.9	0.9	-4.3
13	Brick	NW/SE building/tree	0.30	0.78	0.06	2.8	20.6	-1.7	-0.6	55.4	0.4	6.3	43.3	-1.7	2.9	51.9	0.8	12.25	-1.7	-3.0	-2.9	61.0	0.0	-1.8
14	Asphalt	NW/SE canyon	0.14	0.94	0.17	0.1	5.6	-1.6	-2.2	54.6	0.3	0.9	-1.9	-1.8	-2.9	51.5	0.0	-1.21	-2.2	-3.0	-2.7	60.3	0.6	-4.8
15	Concrete	Tunnel	0.01	0.99	0.09	0.0	-2.8	-1.6	-2.2	54.6	0.4	-3.0	-4.4	-1.9	-2.4	51.5	0.0	-2.23	-0.1	-2.9	-2.3	60.4	0.5	-3.3
16	Brick	NW/SE tree/glass	0.48	0.77	0.08	0.1	1.5	-1.8	-5.8	54.5	0.7	0.2	-2.6	-2.3	-7.2	51.2	0.9	-1.79	-7.4	-3.0	-6.6	59.8	0.5	-3.8
17	Brick	NE/SW canyon	0.50	0.78	0.01	2.8	-3.9	-2.0	-5.7	54.7	1.5	-7.3	-2.0	-2.4	-5.6	52.3	1.3	-3.64	-8.1	-3.0	-6.5	59.6	1.0	-7.5
18	Snow/concrete	NW/SE canyon	0.42	0.80	0.26	0.7	-0.3	-2.1	-4.4	55.5	0.6	-3.8	9.5	-2.5	-3.6	52.6	1.1	-5.94	-9.3	-3.1	-6.2	60.1	0.3	-5.3
19	Concrete	-	0.76	0.62	0.03	7.8	25.3	-1.7	0.0	54.8	0.2	9.7	45.9	-2.0	1.4	52.1	0.3	17.53	-9.9	-3.0	-5.3	59.7	0.3	-4.9
20	Concrete	Tree	0.42	0.53	0.17	5.0	25.8	-1.7	1.9	54.0	1.4	6.3	46.4	-1.9	3.6	51.0	1.2	13.07	-9.5	-3.2	-3.3	59.7	1.7	-9.8
21	Asphalt	-	0.83	0.57	0.04	6.8	23.3	-1.7	-3.3	54.2	1.3	2.8	43.6	-1.9	-2.7	51.5	1.3	6.995	-10.2	-3.2	-7.2	60.0	1.4	-12.7
22	Snow	-	0.80	0.59	0.38	7.7	19.4	-1.7	-7.2	54.1	0.7	5.1	46.6	-1.9	-5.3	51.7	0.0	17.85	-11.6	-3.2	-10.5	59.9	0.7	-9.2
23	Snow	Tree	0.69	0.63	0.44	6.7	21.4	-1.6	-6.8	54.0	0.3	7.9	44.8	-1.6	-3.4	50.4	0.2	17.24	-10.1	-3.2	-10.3	60.0	0.3	-5.1

Legend: Highest | 2nd Highest | 3rd Highest | Lowest

2. Methodology

2.1. Measurement platform

Hourly measurement transects were conducted using a mobile human-biometeorological platform (*MaRTy*; Middel & Krayenhoff, 2019; Fig. 1). The *MaRTy* cart was constructed in Guelph before data collection, mainly following the design of Middel and Krayenhoff (2019) but with select differences in instruments (Fig. 1; also see detailed description of differences in Aiello, 2022).

The cart recorded air temperature (T_a [°C]); relative humidity (*RH* [%]); wind speed (v [m s^{-1}]); location (*lat/lon* [°]); and shortwave (K_i [W m^{-2}]) and longwave radiation (L_i [W m^{-2}]) in a three-dimensional, six-directional format (Ali-Toudert & Mayer, 2007; Höppe, 1992). Ground surface temperature (T_{sfc}) is also reported as the radiative surface temperature based on measurements from a handheld FLIR infrared scanner, assuming an emissivity of 0.95. Fig. 1 contains the specifications of the meteorological instruments used. Greater detail regarding instruments and justification for their use are found in Aiello (2022).

2.2. Study area

Guelph, Ontario (43°33′N 80°15′W) is a city with a population of approximately 130,000 located about 100 km west of Toronto, in the regional vicinity of several Great Lakes. Guelph has a Köppen climate classification of *Dfb*, with cold winters and warm, humid summers, and high amounts of precipitation throughout the year (Ahrens & Henson, 2013). Guelph averages 931 mm of yearly precipitation (rain and snow), and monthly temperature averages range from -6.9 °C in January to 19.7 °C in July, with a yearly average of 1.6 °C (Government of Canada, 2020).

Observations were collected on the University of Guelph's main campus (43° 32′ 0″ N, 80° 13′ 25″ W), which is laid out on a NW/SE-NE/SW orthogonal grid. The campus has 412 hectares of open midrise buildings and forest, including 165 hectares of arboretum land and a 12-hectare research park (University of Guelph, 2013).

2.3. Measurement protocols

Microclimate data were collected during measurement loops at the University of Guelph's main campus on September 15, 2020, November 28, 2020, February 3, 2021, and June 6 and 10, 2021 (note that select measurements were also conducted on June 10, 2021 to supplement the June 6 measurements; see Supplementary Sect. 1). These measurement days were selected to capture a substantial fraction of the seasonal variation in key climate variables during clear skies, such as air temperature, solar angle and snow cover, in a southern Ontario city.

Measurement loops were completed in approximately 40 minutes at a walking pace with stops at each of 23 locations around campus (Fig. 2) in summer and autumn, with observations logged every 2 seconds. Only 21 locations were sampled during winter loops; locations 6 and 7 were bypassed during this season because the entryway to the courtyard in which they were located was blocked by construction equipment. Tables 1 and 2 contain details of each site, and additional details related to shade (e.g., tree species) are found in Aiello (2022). Hourly measurement loops began in the late morning and ended approximately two hours after sunset, with select hours as designated breaks. Thus, 6–9 loops were completed on each measurement day. Stop locations and associated cart orientation were indicated by chalk markings to ensure measurement consistency. The cart was stopped for 45 s to account for sensor response time (specifically the radiometers) and ensure that several measurements were taken after sensor adjustment to the new conditions at each location and time (Häb et al., 2015). All observations were linearly interpolated to a fixed time based on measurements conducted during the hour immediately prior and after the fixed time, for temporal consistency across sites (Aiello, 2022; Middel & Krayenhoff, 2019).

Sensor views were visualized and quantified using fisheye photographs taken with a Nikon Coolpix 880 and a Nikon FC-E8 Fisheye Converter 8mm lens in each cardinal direction (lateral) and facing upwards (hemispherical). These images were used to quantify each location's directional view factors of various urban elements and features (impervious, pervious, sky, snow).

Site locations measured in June, September, and November were chosen based on their combined surface type (asphalt, brick, concrete, grass) and shade type (artificial/natural, complete/partial) to capture diverse urban micro-environments. In February, snow and ice accumulation and the lack of deciduous tree foliage exemplified key seasonal changes to urban spaces in continental climates. Some sites previously located on grass or concrete surfaces became classified as snow surfaces. Frequently used walkway surfaces made of asphalt and brick had been cleared of snow before the measurement day. Additional details are available in Aiello (2022).

2.4. Mean radiant temperature and thermal stress indices

Only stationary observations were analyzed. The GPS sensor recorded movement speed, and any records containing motion were removed from the analysis. Subsequently, the first 10 and last 5 data points (20 and 10 seconds, respectively) of each 45–60 s stationary observation period were removed to account for sensor response time as well as any instances where the operator may have influenced a sensor reading as they approached the cart to move it to the following observation location. Finally, observations were linearly interpolated to selected hours based on measurements conducted immediately before and immediately after the time stamp for temporal consistency across sites (Middel & Krayenhoff, 2019). For additional details on interpolation methods, see Aiello (2022).

T_{mrt} [°C] was calculated from three-dimensional shortwave (K_i) and longwave (L_i) observations at each location with weightings W_i applied to represent a standing reference pedestrian (VDI 1998):

$$T_{mrt} = \sqrt[4]{\frac{\sum_{i=1}^{6} W_i(a_k K_i + a_l L_i)}{a_l \cdot \sigma}} - 273.15, \quad (1)$$

where $a_k = 0.70$ and $a_l = 0.97$ are the short- and longwave radiant flux density absorption coefficients of the pedestrian, respectively, σ is the Stephan-Boltzmann constant $\left(5.67 \times 10^{-8}\ W{\cdot}m^{-2}{\cdot}K^{-4}\right)$, $W_i = 0.06$ for the up and down sensors, and $W_i = 0.22$ for the sensors pointing in each cardinal direction (VDI, 1998).

Once T_{mrt} was calculated, the thermal comfort indices Physiologically Equivalent Temperature (*PET*) (Höppe, 1999) and Universal Thermal Climate Index (*UTCI*) (Jendritzky et al., 2012) were computed. *PET* was calculated by inputting T_a, *RH*, v, T_{mrt}, and physical attributes representing the conditions of each season into RayMan Pro (Matzarakis et al., 2007, 2010), where a walking 1.7 m tall 35-year-old male was set as the default reference pedestrian. *UTCI* was calculated in R (Crisci & Morabito, 2016). Surface level wind speed (1.8m) measured by the *MaRTy* cart was converted into a wind speed height required by the *UTCI* calculation using Eq. 2, defined by Bröde et al. (2012) as a component in the optimal procedure for *UTCI*:

$$v_a = v_{xm}\left(\frac{\log(10\ /\ 0.01)}{\log(x\ /\ 0.01)}\right), \quad (2)$$

where v_a represents the 10m wind speed required to calculate *UTCI*, v_{xm} represents wind speed measured at x [m] height, and 0.01 represents the roughness length. This approach gives the UTCI algorithm the 10 m wind speed that will yield the actual measured wind speed at the pedestrian level within its calculations.

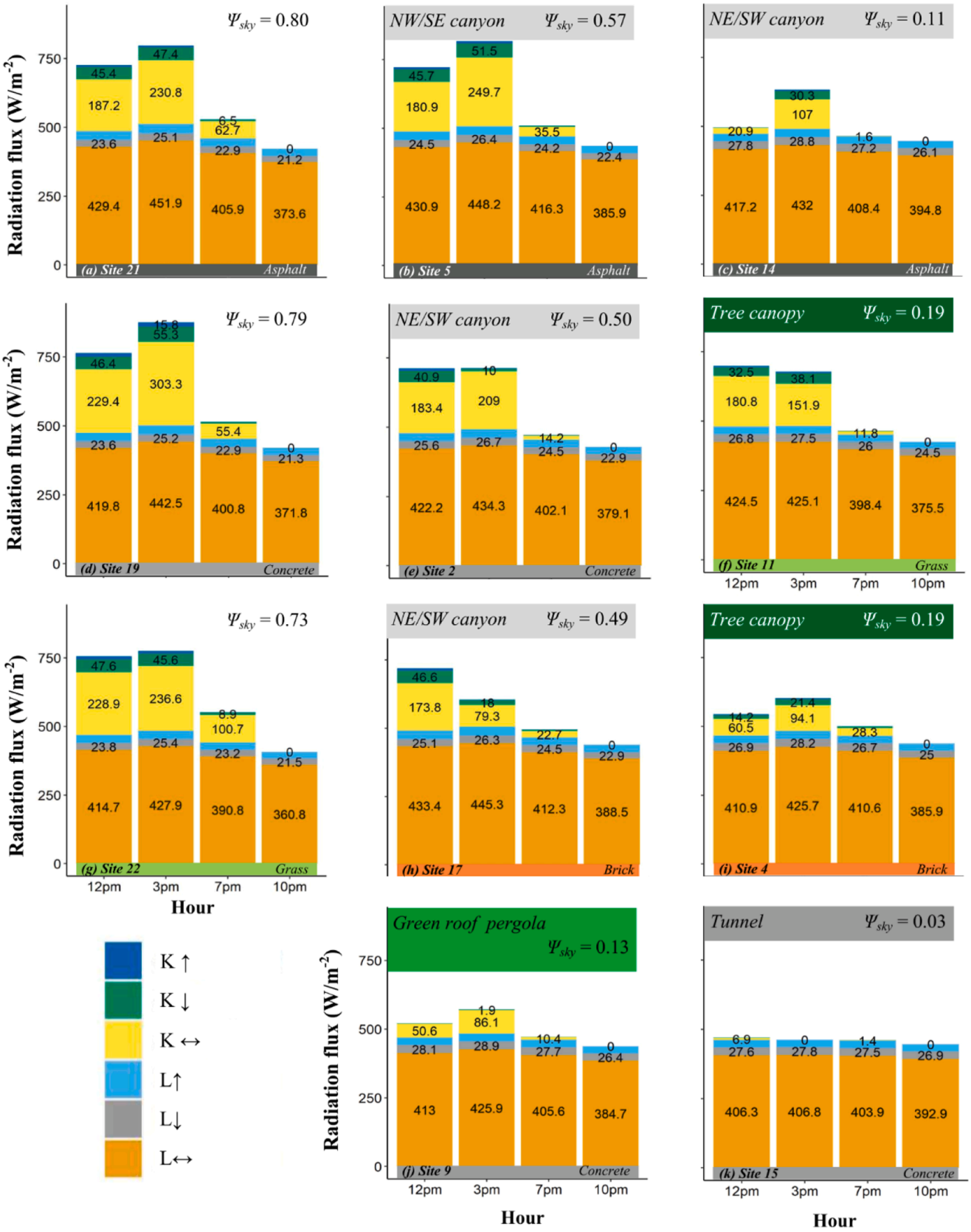

Fig. 3. Directionally-weighted radiation fluxes absorbed by a pedestrian during June 6th, 2021 at a selection of sites, illustrating the magnitude of longwave (*L*) and shortwave (*K*) fluxes that contribute to mean radiant temperature (T_{mrt}). Associated microscale site characteristics are identified at the top and bottom of each plot.

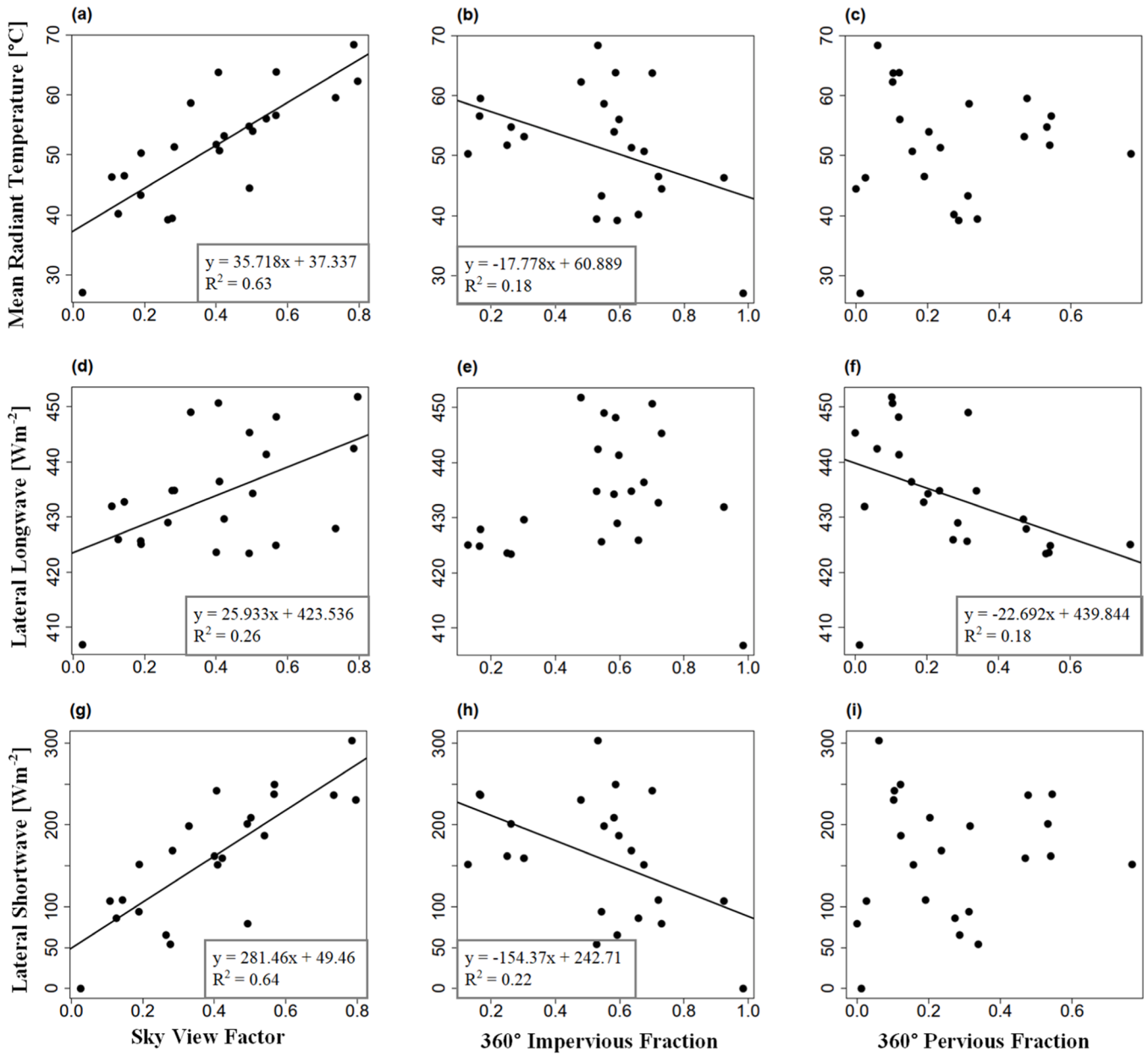

Fig. 4. Mean radiant temperature (T_{mrt}), lateral longwave (L_{lat}), and lateral shortwave (K_{lat}) radiation fluxes plotted against physical characteristics influencing urban microclimate during mid-afternoon (15:00 EDT) on June 6, 2021. Linear regression best fit lines, equations, and coefficients of determination are included where $p < 0.05$.

2.5. View factors of environmental components

Sky view factor (Ψ_{sky}), lateral impervious view factor (I_{360}), lateral pervious view factor (P_{360}), and lateral snow view factor (Sn_{360}) were determined by manually processing the upward-facing and four lateral hemispherical fisheye photos. In summer, each fisheye photo was segmented into sky, impervious, and vegetation, and Ψ_{sky}, I_{360}, and P_{360} (upward sky, lateral sky, lateral impervious, and lateral pervious view factors, respectively) were estimated using RayMan (Matzarakis et al., 2007, 2010), which analyzed each segmented fisheye photo. Sites were then further classified based on their view factor values. In winter, Ψ_{sky}, I_{360}, and P_{360} were found with the same method using an additional set of fisheye photographs taken in late January 2021 to account for the presence of snow and the loss of leaves from trees. For this season, snow cover is assessed based on photo segmentation, allowing for the estimation of Sn_{360} using RayMan. Sn_{360} quantifies the view factor of snow from the lateral fisheye photos and cannot account for the depth of accumulated snow. For a detailed description of image processing, see Aiello (2022). The analysis of upward-facing fisheye photographs in RayMan (Matzarakis et al., 2010, 2007) was also used to obtain sunlight hours experienced by each site and solar elevation and azimuth angles associated with the time of day and year when measurements were gathered.

3. Results

3.1. Heat exposure during an extreme heat day (June 6, 2021)

3.1.1. Meteorological observations

June 6, 2021 was the warmest day of the month and was the highest observed air temperature at the Guelph Turfgrass Weather Station June 6 since 1925. During the 1500 EDT measurements at the University of

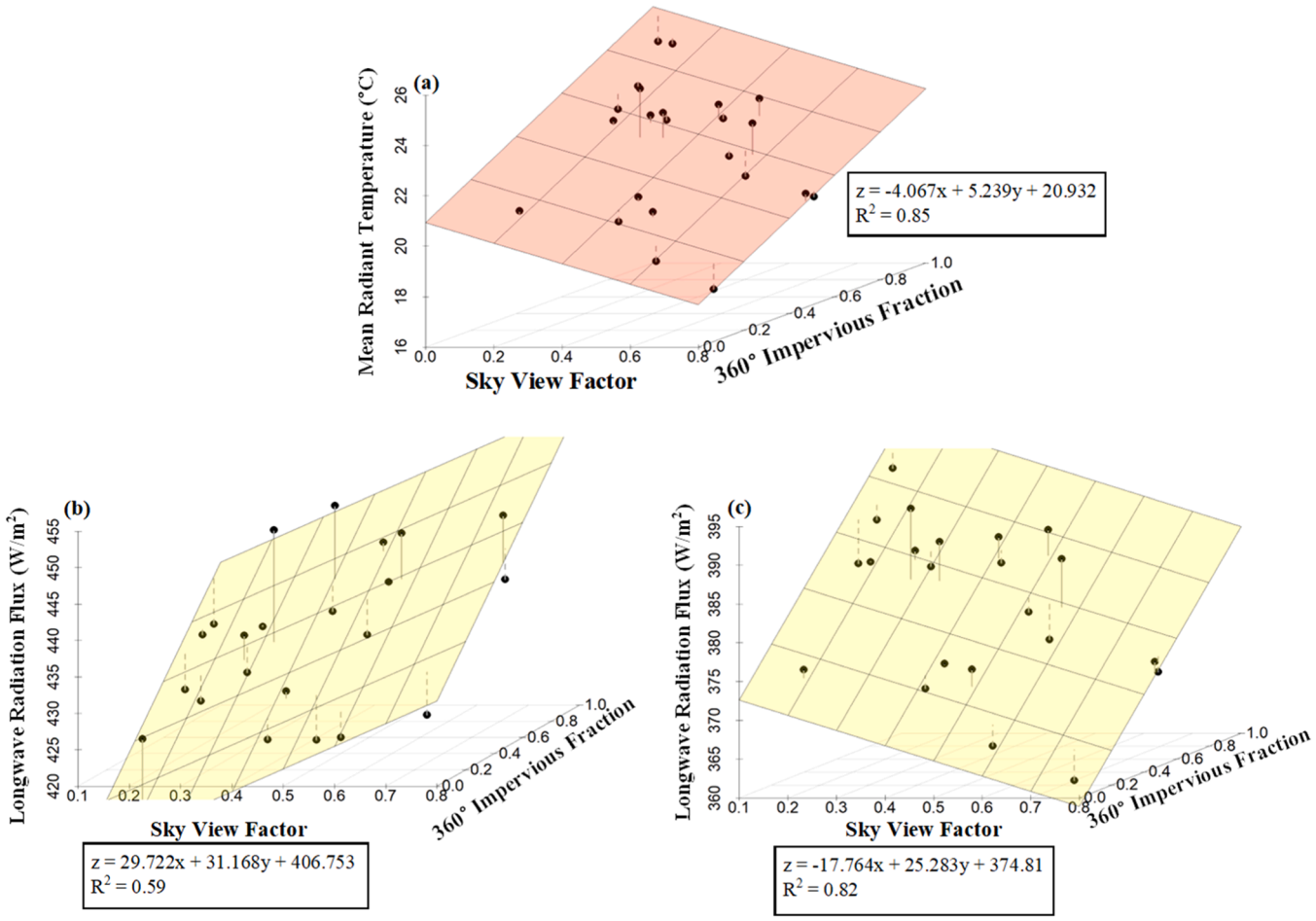

Fig. 5. Multiple linear regression of *Tmrt* and its components against land cover and sky view factors. (a) Mean radiant temperature (T_{mrt}, z-axis) as a function of Ψ_{sky} (x-axis) and I_{360} (y-axis) at night (22:00 EDT); (b) L_{lat} (z-axis) as a function of sky view factor (Ψ_{sky}, x-axis) and lateral impervious view factor (I_{360}, y-axis) in the afternoon (15:00 EDT); and (c) L_{lat} as a function of Ψ_{sky} (x-axis) and I_{360} (y-axis) at night (22:00 EDT) on June 6th, 2021. $p < 0.05$ in all cases shown.

Guelph's main campus, T_a peaked at 31.9 °C (site 23, $\Psi_{sky} = 0.57$) over dry grass and under partial tree cover adjacent to an asphalt parking lot (Table 1). The minimum T_a at 1500 EDT was 30.7 °C at site 4 ($\Psi_{sky} = 0.19$), over brick and under dense tree shade.

At 1500 EDT, the highest recorded surface temperature (T_{sfc}) was 53.5 °C (site 21, $\Psi_{sky} = 0.80$) over asphalt, and the lowest recorded T_{sfc} was 22.1 °C, in a concrete tunnel (site 15, $\Psi_{sky} = 0.03$; Table 1). T_{mrt} peaked at site 19 ($\Psi_{sky} = 0.79$) with an observed value of 68.4 °C over concrete and adjacent to a short building with a glass façade. This measurement was 41.3 °C higher than the lowest T_{mrt} reading at 1500 EDT: 27.1 °C at site 15, an enclosed concrete tunnel ($\Psi_{sky} = 0.03$).

Variability between relative humidity (*RH*) measurements at each site was low (±1.6%) throughout the day due to atmospheric mixing and the small study area (0.10 km^2). Wind speed (v) measurements for all sites during daytime (1200–2200 EDT) ranged from 0.07 m s^{-1} to 2.26 m s^{-1}.

3.1.2. Thermal stress and comfort indices

During the June 6 measurement period, *UTCI* reached a maximum value of 40.2 °C at site 19, corresponding to the highest T_{mrt} observation (68.4 °C; Table 1). The largest *PET* observed was 49.3 °C at site 5, an asphalt road surface in an NE/SW building canyon. Differences between *UTCI* and *PET* were as high as 10.9 °C, with an average difference of 5.3 °C during the daytime peak, likely resulting from the adaptive clothing model included in the *UTCI* model (Havenith et al., 2012) but not in the RayMan version of the *PET* model, which assumes a constant clothing factor (*clo*) of 0.8.

3.1.3. Controls on T_{mrt} and directional radiation

T_{mrt} largely controls the spatial variation of UTCI and PET for warm sunny conditions. Thus, the variation of T_{mrt} is further investigated. Fig. 3 presents directionally weighted radiation fluxes that would be absorbed by a pedestrian (i.e., their magnitude represents their contribution to T_{mrt}) at 11 sites. Measured radiation fluxes unweighted by the relative exposure of the pedestrian to the environment (i.e., larger in lateral directions) are found in Aiello (2022). Most longwave radiation arrives from lateral directions, and absorption of longwave radiation was approximately five to ten times the magnitude of absorbed shortwave radiation in full tree shade, decreasing to approximately twice the magnitude in direct sun (Fig. 3). Shortwave radiation data fluctuated spatially and temporally, dependent on the presence and location of the sun in the sky, with longwave radiation fluxes remaining more constant over time and varying primarily with differences in ground cover and shade provision.

During the day (1500 EDT), shaded sites received limited shortwave radiation, while at night, these same locations increased longwave radiation absorption after sunset (Fig. 3). During the day, shaded T_{mrt} values were up to 16 °C lower under building cover (over asphalt) compared to unshaded locations (Fig. 3a,c; sites 14 and 21 in Table 1), and 9 °C less under tree shade (over grass) relative to unshaded locations (Fig. 3f,g; sites 11 and 22 in Table 1). Trees permitted diffuse infiltration of shortwave radiation to the surface, providing less complete shade than buildings. The effects of extreme impervious cover and shade occur at site 15 (tunnel), where absorbed longwave radiation and T_{mrt} are relatively unchanged over the measurement period (Table 1, Fig. 3k).

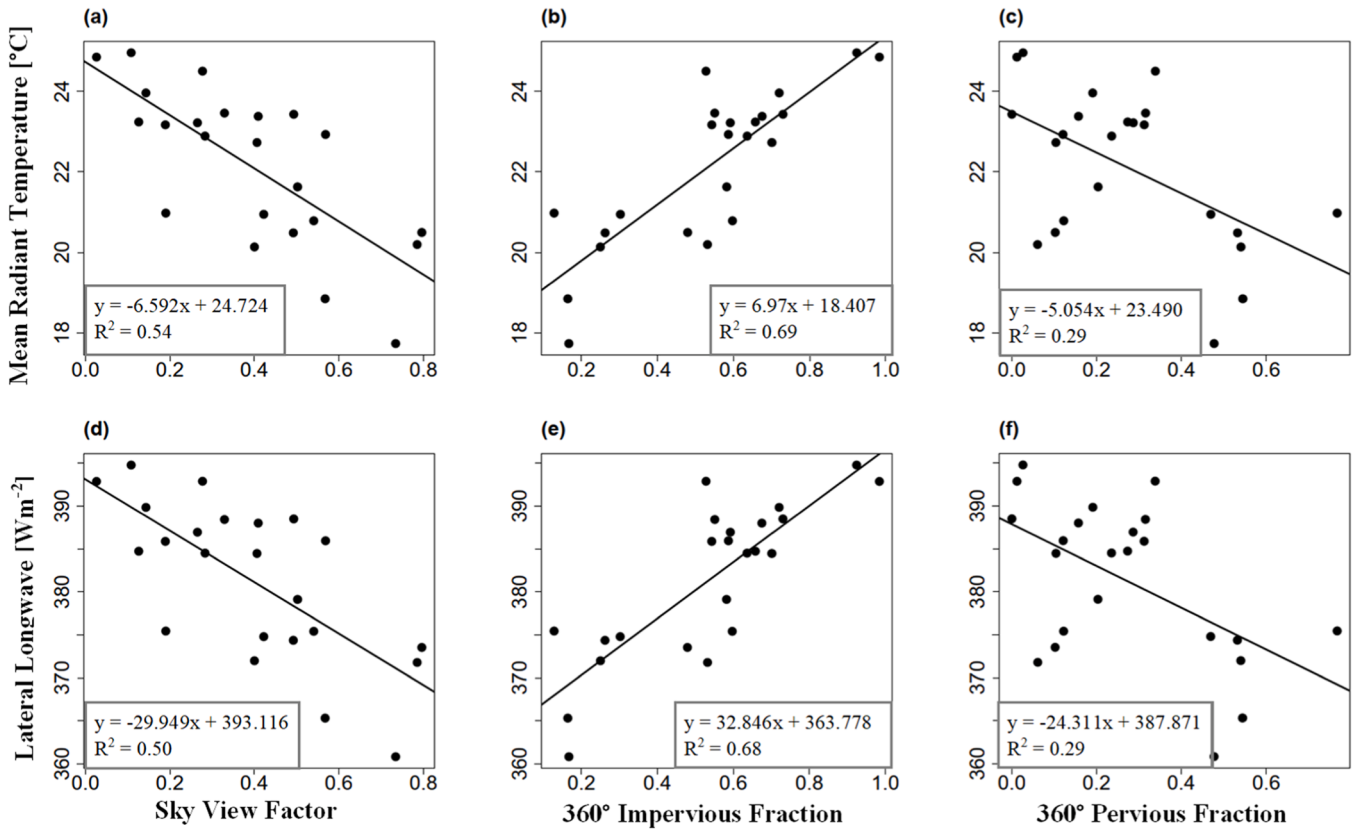

Fig. 6. Mean radiant temperature (T_{mrt}), lateral longwave (L_{lat}), and lateral shortwave (K_{lat}) radiation fluxes plotted against physical characteristics influencing urban microclimate during nighttime (22:00 EDT) on June 6th, 2021. Linear regression best fit lines, equations, and coefficients of determination are included where $p < 0.05$.

Impervious surfaces, particularly asphalt (sites 14 and 21; Fig. 3a,c), exhibited elevated emissions of longwave radiative fluxes relative to open grass surfaces (sites 11 and 22, respectively; Fig. 3f,g), even when shaded during the day. At night (2200 EDT), T_{mrt} over concrete and asphalt sites remained 3–4 °C warmer than grass due to higher longwave emission from the surface (Table 1; Fig. 3).

3.1.4. *Impacts of surface structure and cover on T_{mrt}*

Simple and multiple linear regression models are developed to explain T_{mrt} and its primary drivers, absorbed lateral longwave radiation (L_{lat}) and absorbed lateral shortwave radiation (K_{lat}), as a function of sky (Ψ_{sky}), lateral impervious (I_{360}) and lateral pervious (P_{360}) view factors. View factors of thermally distinct radiative emitters are chosen as explanatory variables. Information on the development of these statistical models can be found in Aiello (2022).

During midday (1200 EDT) and mid-afternoon (1500 EDT), the sky view factor (Ψ_{sky}) best explained T_{mrt} and K_{lat}, because Ψ_{sky} is inversely related to shade (Supplementary Fig. 2; Fig. 4). By 1500 EDT, Ψ_{sky} also had a significant positive relationship with L_{lat} because open surfaces absorb more direct solar radiation and therefore emit more longwave radiation. T_{mrt} and K_{lat} were negatively correlated with I_{360} since the latter comprised buildings that provided shade. Multiple regression of L_{lat} against both Ψ_{sky} and I_{360} yields a much stronger signal (Fig. 5b) since Ψ_{sky} serves to discriminate between sites with substantive impervious structure, such as buildings, which provide shade and cooler daytime surface temperatures, versus areas with higher impervious cover at ground level, such as roads and parking lots, which heat up in the mid-afternoon sun.

After sunset, L_{lat} explained the majority of variability in T_{mrt} (Fig. 6). I_{360} was the best single predictor of T_{mrt} and L_{lat}, indicating that vertical and horizontal impervious surfaces emit more longwave radiation than pervious surfaces and the sky, contributing to a higher T_{mrt}. Ψ_{sky} was negatively correlated with both T_{mrt} and L_{lat}, as expected. P_{360} also had negative correlations in T_{mrt} and L_{lat} due to the relative coolness of pervious grass surfaces. The warming effect of I_{360} was clearer when included as a predictor with Ψ_{sky} in multiple linear regression. These two variables explained most of the variability in T_{mrt} (Fig. 5a), with the majority of this explanatory power stemming from the corresponding relation for L_{lat} (Fig. 5c).

3.2. *Winter cold exposure during a clear sky day (Feb. 3, 2021)*

3.2.1. *Meteorological observations*

The diurnal maximum and minimum air temperatures observed at the University of Guelph Turfgrass weather station on February 3, 2021, were -0.2 °C and -9.6 °C, respectively. During the measurement period at the University of Guelph's main campus, the *MaRTy* cart recorded T_a reaching 0.0 °C at 1500 EST (site 22) and dropping as low as -3.3 °C after sunset (site 4; Table 2). Despite much lower moisture content in the air, *RH* in February was greater than in June. The average measurement for all sites combined ranged from 51.5% at midday to 60.3% after sunset (Table 2).

The warmest T_{sfc} observation was 5.4 °C at site 20 ($\Psi_{sky} = 0.42$) above a concrete sidewalk at 1500 EST. Sites with snow surfaces experienced the coldest T_{sfc} readings after sunset and reached minimum observed temperatures of -10.5 °C, -10.3 °C, and -7.9 °C (sites 22, 10, and 23, respectively) (Table 2). T_{mrt} peaked at 46.8 °C at a site over snow and under a partial coniferous tree canopy (site 11, $\Psi_{sky} = 0.41$) at 1200 EST. T_{mrt} varied by 51.2 °C between the warmest and coldest sites (sites 11 and 15, respectively) at this time, where site 15 was the concrete tunnel that received negligible sunlight throughout the day. After sunset, site 15 had the highest T_{mrt} (0.1 °C), while the lowest T_{mrt} (-11.6 °C)

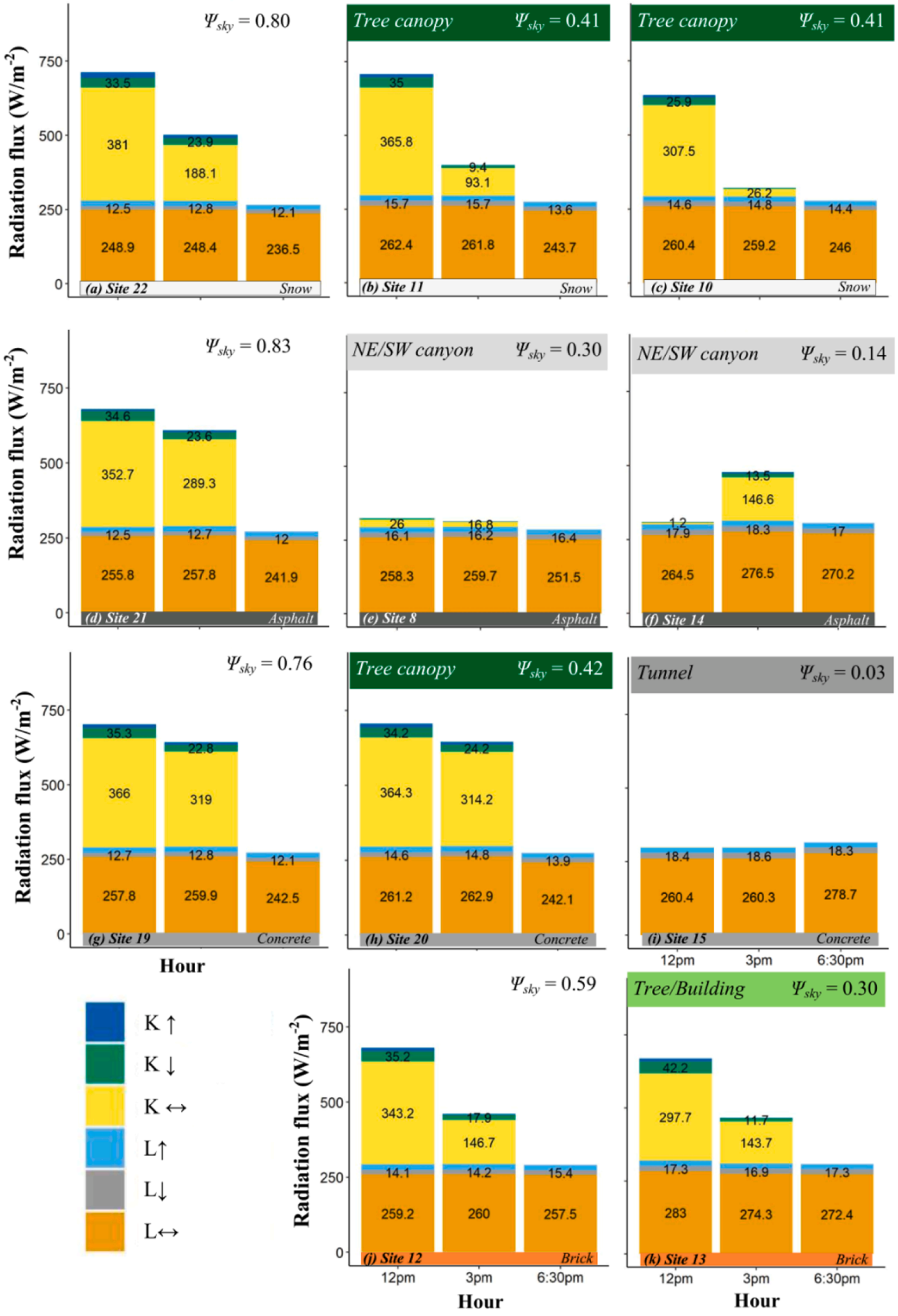

Fig. 7. Directionally-weighted radiation fluxes absorbed by a pedestrian at a selection of sites during February 3rd, 2021 illustrating the magnitude of longwave (L) and shortwave (K) radiation fluxes that contribute to mean radiant temperature (T_{mrt}). Associated microscale site characteristics are identified at top and bottom of each plot.

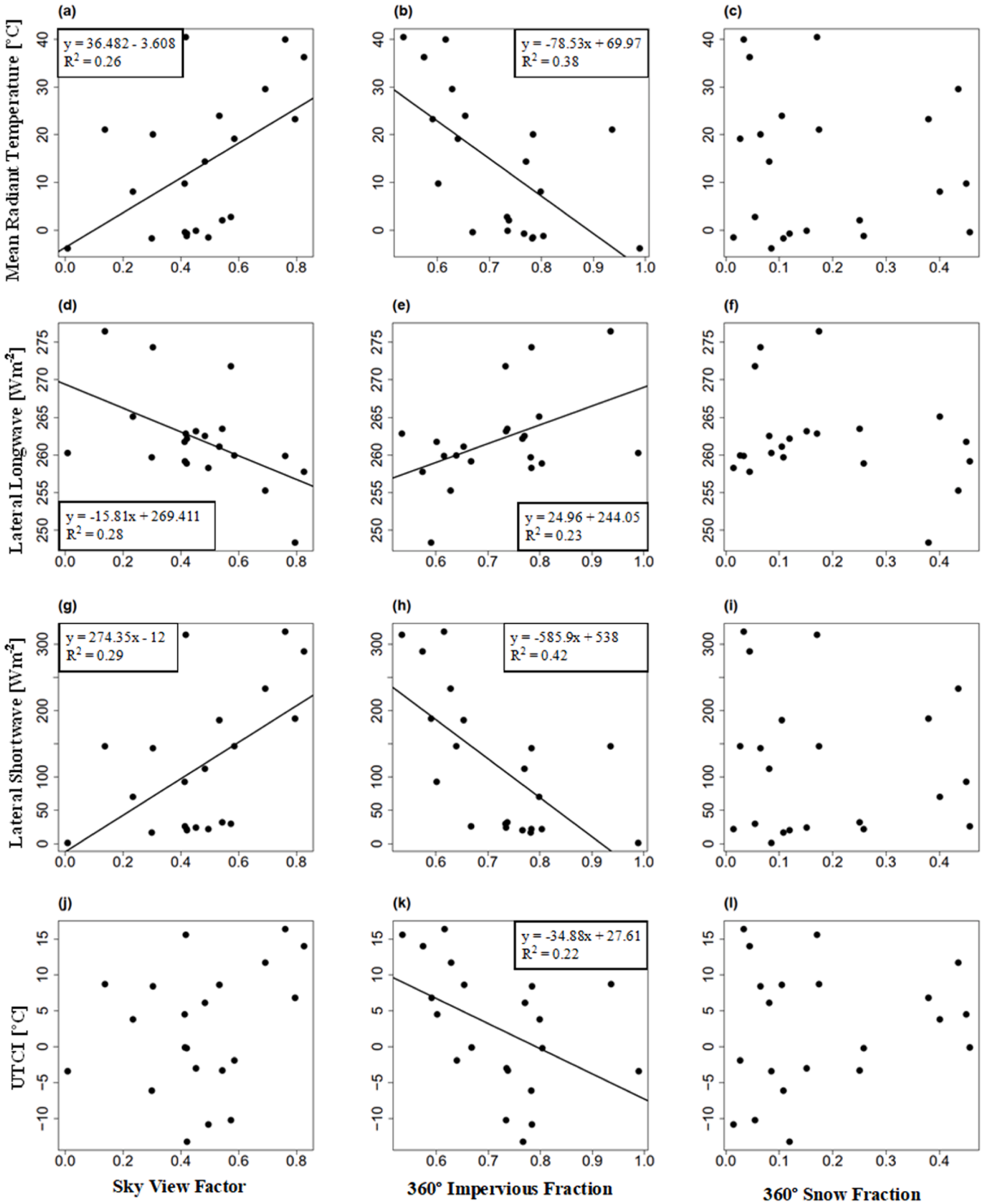

Fig. 8. Mean radiant temperature (T_{mrt}), lateral longwave flux (L_{lat}), lateral shortwave flux (K_{lat}), and the Universal Thermal Climate Index (*UTCI*) plotted as a function of sky view factor (Ψ_{sky}), lateral impervious view factor (I_{360}), and lateral snow view factor (Sn_{360}) during mid-afternoon (15:00 EST) on February 3rd, 2021. Linear best fit lines and associated equations are plotted for panels where $p < 0.05$.

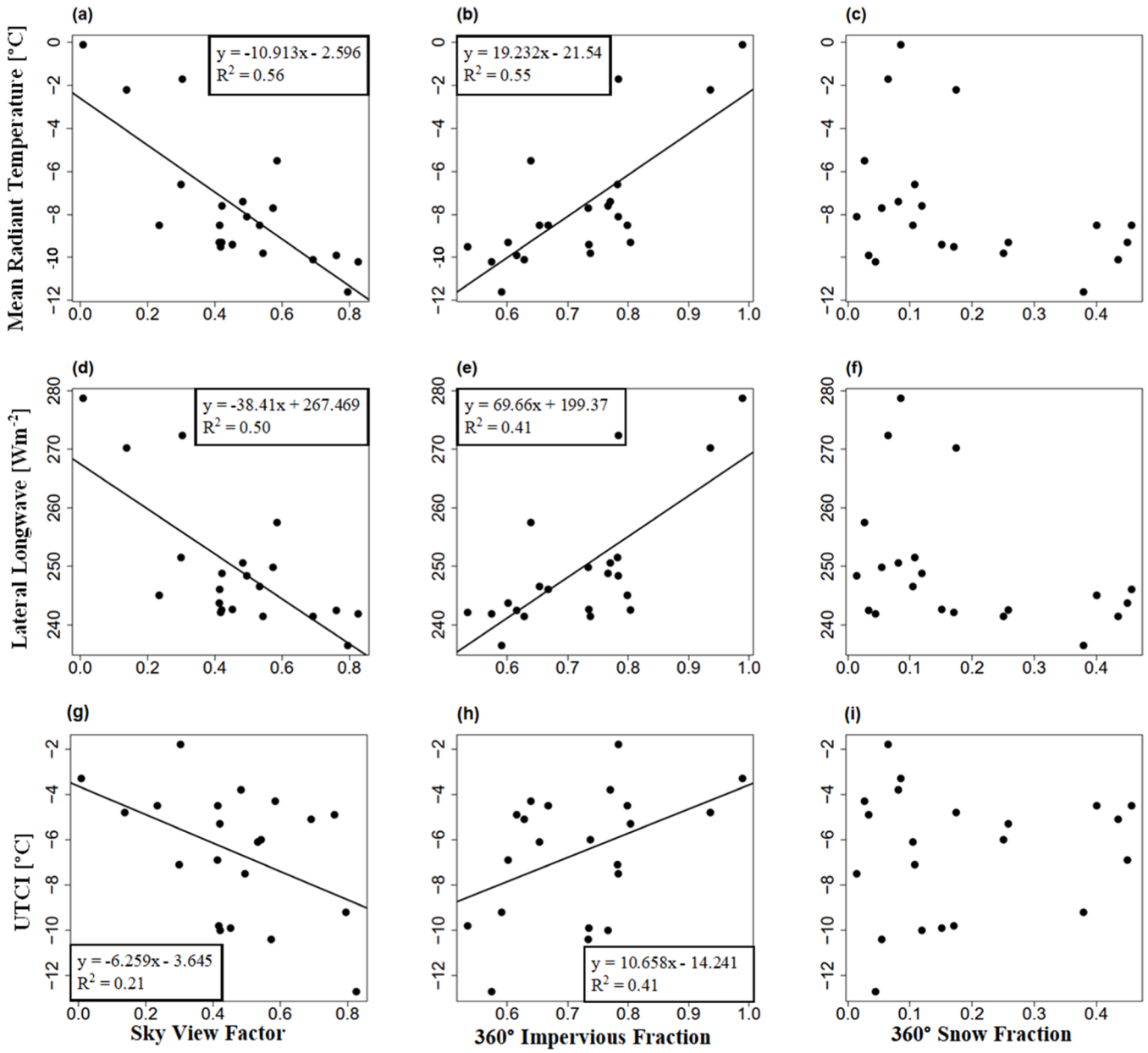

Fig. 9. Mean radiant temperature (T_{mrt}), lateral longwave flux (L_{lat}), lateral shortwave flux (K_{lat}), and the Universal Thermal Climate Index (*UTCI*) plotted as a function of sky view factor (Ψ_{sky}), lateral impervious view factor (I_{360}), and lateral snow view factor (Sn_{360}) during nighttime (18:30 EST) on February 3rd, 2021. Linear best fit lines and associated equations are plotted for panels where $p < 0.05$.

was an open, snow-covered location (site 22; $\Psi_{sky} = 0.80$; Table 2).

In winter, wind speed often plays a critical role in determining thermal exposure, though not always (Xiong & He, 2022; Xu et al. 2018); thus, T_{mrt} alone is often less effective for determining pedestrian thermal exposure variability than in the summer. Wind speed varied between sites during the measurement period. The highest v was 3.6 m s^{-1} in a narrow sidewalk canyon (site 3) at 1500 EST. Early afternoon and night measurements fell below 1 m s^{-1} (Table 2).

3.2.2. Thermal stress and comfort indices

During the February 3rd measurements, *UTCI* reached a maximum value of 18.0 °C during 1500 EDT at site 11, a snow-covered site with modest tree cover and good southern exposure (Table 2 and Fig. 2). The lowest *UTCI* value was observed at site 8 during midday (-13.0 °C) due to shady and windy conditions ($v = 2.8$ m s^{-1}) in that canyon (Table 2).

3.2.3. Controls on T_{mrt} and directional radiation

While wind speed, air temperature, and humidity are important controls on wintertime cold stress, we focus here on T_{mrt} during conditions where it is likely a substantial contributor to the spatial variation of thermal stress: clear skies and light winds. Snow cover decreased T_{sfc} at site 22 by 2.5–7.0 °C during the daytime radiative peak (1200 EST) relative to comparable but snowless sites 19 and 21, resulting in a lower L_{lat} (Table 2, Fig. 7a,d,g). At this time, the high albedo of the snow at site 22 ($\alpha \approx 0.50$) yielded increased contributions to K_{up} and K_{lat}, exceeding the decrease in absorbed longwave radiation due to the lower surface temperature of snow, contributing to a relatively high T_{mrt} of ~45 °C at this site, as well at three other sites with different ground covers that also received full sun exposure (12, 19, 21; Fig. 7a,d,g,j).

After sunset (18:30 EST), T_{sfc} of the snow at site 22 was 5 °C colder than the T_{sfc} of asphalt, concrete, and brick surfaces (Table 2). Site 22 had the lowest T_{mrt}, 1.5 °C to 6 °C lower than other open, impervious

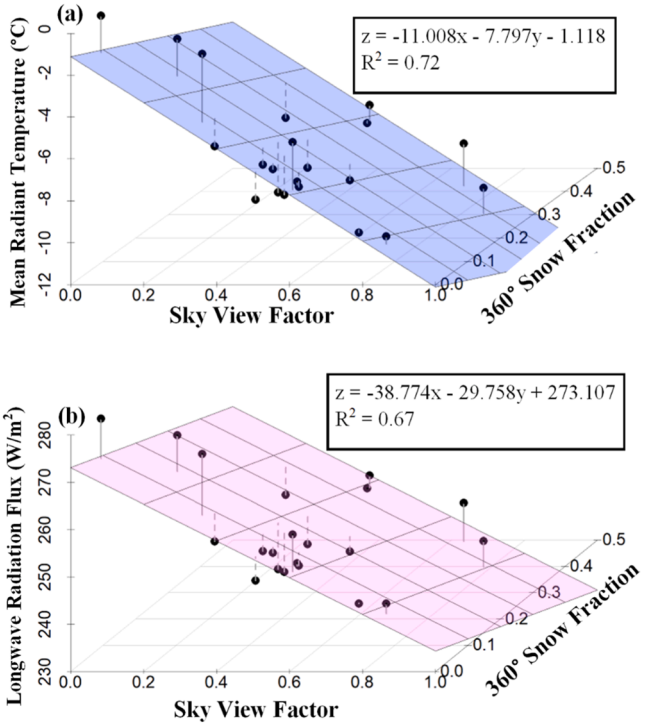

Fig. 10. (a) Mean radiant temperature (T_{mrt}, z-axis) as a function of sky view factor (Ψ_{sky}, x-axis), and lateral snow view factor (Sn_{360}, y-axis); (b) lateral longwave radiation flux (L_{lat}, z-axis) as a function of Ψ_{sky} (x-axis) and Sn_{360} (y-axis), with 2D regression planes visualizing the multiple linear regression equations and coefficient of determination (R^2) after sunset (18:30 EST) on February 3rd, 2021. $p < 0.05$ for both regressions.

sites. It was the most thermally uncomfortable site with snow on the ground (*UTCI* is 5 °C lower than at site 10, which is also snow-covered but with lower Ψ_{sky} due to the proximity of buildings and trees; Table 2). After sunset, sites with large I_{360} values exhibited relatively high L_{lat} values (Fig. 7). For example, sites 14 and 15 (Fig. 7f,i), whose lateral impervious view factors were 94% and 99%, respectively, had higher *UTCI* values (-4.8 °C and -3.3 °C, respectively) compared to the average across sites (-6.6 °C).

Overall, sites that received direct sunlight during the day and effectively reflected it back up toward the pedestrian (e.g., sites with snow cover) were the most thermally comfortable. However, these sites also resulted in the greatest cold exposure after sunset. Sites with direct sunlight exposure and partial canopy cover better moderated thermal exposure day and night (e.g., site 13).

3.2.4. Impacts of surface structure and cover on T_{mrt}

Simple and multiple linear regression models were created to associate variables quantifying thermal exposure (T_{mrt}, *UTCI*, L_{lat}, and K_{lat}) with relevant exposures to sky and infrastructure as quantified by Ψ_{sky}, I_{360}, P_{360}, and lateral snow (Sn_{360}) view factors. See Aiello (2022) for more information on development of the statistical models used in February. These models exhibit moderate predictive value, with clearer patterns observed after sunset (Figs. 8-11). Over the measurement period, significance was not observed in simple linear regression models that used Sn_{360}.

During midday and mid-afternoon, building shade as quantified by I_{360}, or conversely solar exposure as captured by Ψ_{sky}, were strong predictors of T_{mrt} (Supplementary Fig. 3; Fig. 8). Thermal exposure was again driven shade, especially during midday, as expressed by the variation of K_{lat} with impervious (i.e. building) fraction (Supplementary Fig. 3; Fig. 8). A more minor effect is the increase of L_{lat} as a function of impervious surface view factor during the afternoon (Fig. 8).

After sunset, I_{360} became the strongest predictor of T_{mrt}, driven by an increase in lateral longwave emitted from buildings and impervious ground cover (Fig. 9). The magnitude of cooling was also strongly associated with Ψ_{sky}, resulting in reduced L_{lat}, which contributed to lower T_{mrt} and *UTCI* values (Fig. 9). Moreover, the combination of Ψ_{sky} and Sn_{360} significantly explained nighttime T_{mrt} reduction, largely due to their impact on lateral longwave radiation, demonstrating that open snowy sites emit less longwave radiation toward the pedestrian at night (Fig. 10). These sites are the coldest sites measured in the current sample.

3.2.5. Snow subsets

A subset of snow-only sites was created by omitting any site with an I_{360} value ten times greater (or more) than its respective value of Sn_{360}. Additional information regarding the snow subset of sites is found in Aiello (2022). Within this subsample, Sn_{360} was a significant predictor of spatial variation of several biometeorological variables between sites at midday (1200 EST), including T_{mrt}, K_{lat}, and *UTCI* (Fig. 11), all of which increased with higher snow cover. These relationships likely result from the relatively high snow albedo ($\alpha \approx 0.50$), which transforms K_{down} into K_{lat} via reflection, and/or from the fact that sites with greater snow cover typically have greater Ψ_{sky} and, therefore, greater sun exposure.

3.2.6. Comparison between cold (Feb. 3) and hot (June 6) day measurements

Solar radiation fluxes in February had a greater absolute and relative impact on pedestrian thermal exposure despite longer daylight hours and higher solar elevation angles in June (15.3h) compared to February (10h), as seen by comparing Figs. 3 and 7. Select sites in February had higher lateral shortwave radiation due to at least two potential factors. First, sites containing snow had a higher surface albedo than any surfaces in June, allowing for the efficient transformation of shortwave radiation incident on nearby snow-covered ground surfaces into K_{lat} via reflection. Second, a lower peak solar elevation in February (27°) compared to June (63°) resulted in a greater contribution to K_{lat}, increasing the solar energy felt by a standing pedestrian whose surface area is mostly vertically oriented. Moreover, colder surface temperatures in February resulted in a reduced magnitude of L_i flux, increasing the relative impact of K_i flux on the reduction of cold exposure.

4. Discussion

We measured three-dimensional shortwave and longwave radiant flux contributions to T_{mrt} for different weather conditions in an urban environment on the main campus of the University of Guelph, Canada (43.53°N, 80.23°W), located in a humid continental zone (*Dfb*). Warm weather observations were consistent with radiation fluxes on pedestrians in other summertime temperate climates at similar latitudes. During July in Freiburg, Germany (48°N), T_{mrt} peaked at 66 °C, and T_a reached a maximum of 35 °C (Ali-Toudert & Mayer, 2007). In August and September in Pécs, Hungary (46.07°N), T_{mrt} reached a maximum of 60 °C (Kántor et al., 2018). Lastly, during July in the high latitude city of Göteborg, Sweden (57.70°N), T_{mrt} peaked near 58 °C, a somewhat smaller value than the observations in temperate climates (Lindberg et al., 2008). In the extreme summertime heat of Tempe, Arizona (33.43°N), T_a reached 48.5 °C while T_{mrt} peaked at 75 °C (Middel & Krayenhoff, 2019). The current measurements found that T_{mrt} displayed the most variation between shaded and sunlit sites in the afternoon ($\Delta T_{mrt} = 41$ °C), followed by surface temperature ($\Delta T_{sfc} = 31$ °C) and air temperature ($\Delta T_a = 1.2$ °C). Middel and Krayenhoff (2019) found similar results except for larger ΔT_a (4.4 °C). Our results highlight the importance of radiative fluxes to the spatial variation of pedestrian thermal exposure and comfort during hot weather in midlatitude summer climates, in line with previous work, and indicate that spatial variation of warm weather (June and September) pedestrian thermal exposure was largely controlled by T_{mrt}, especially in low wind

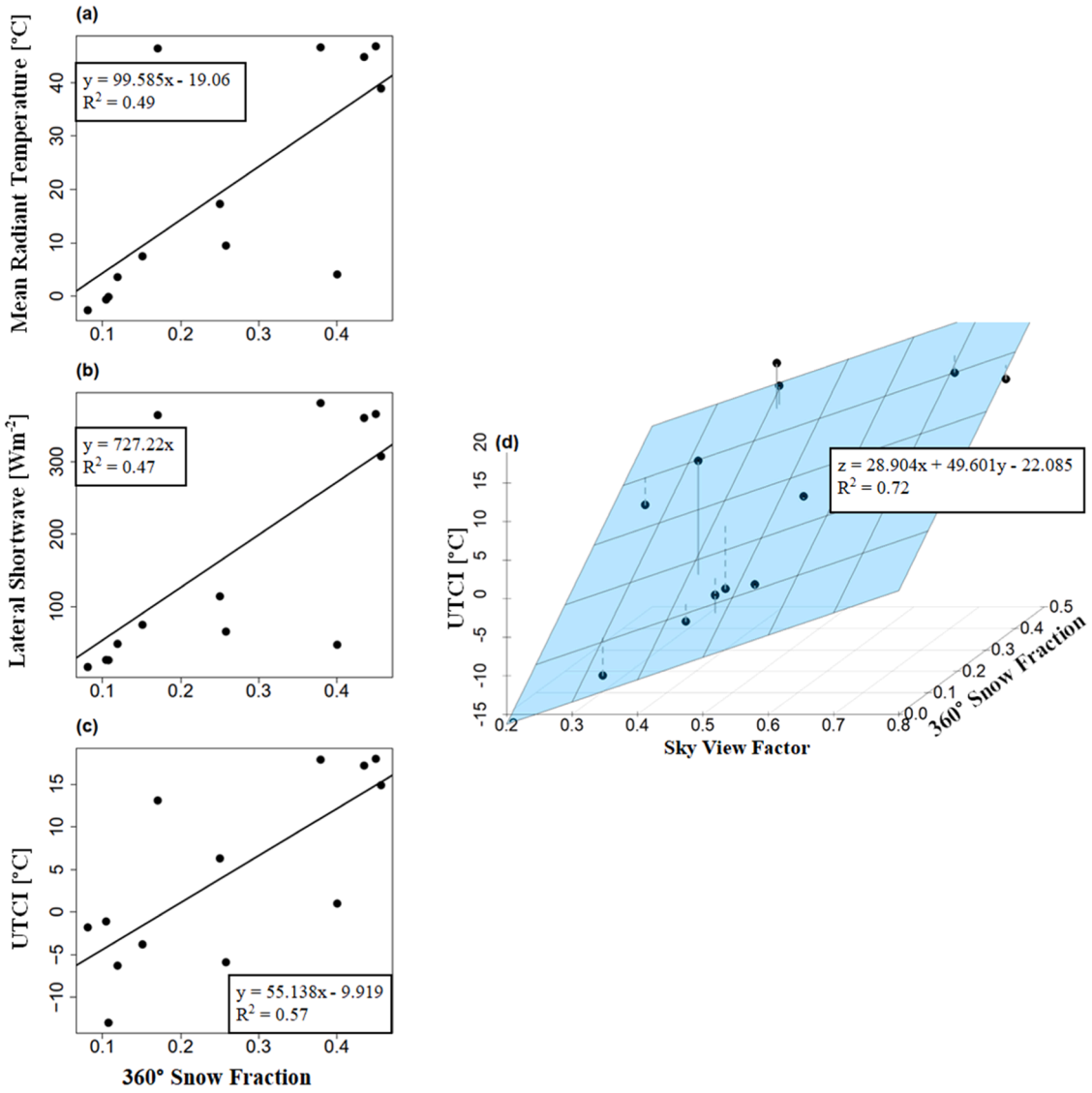

Fig. 11. Simple (a-c) and multiple (d) linear regressions with lateral snow view factor (Sn_{360}) as a predictor of mean radiant temperature (T_{mrt}), lateral shortwave radiation (K_{lat}), and the Universal Thermal Comfort Index (*UTCI*) for a subset of measurement sites during solar maximum (12:00 EST) on February 3rd, 2021. $p < 0.05$ for all regressions.

conditions.

Radiative flux observations taken between November 2017 and January 2018 in Harbin, China present the only other cold-weather study with explicit six-directional radiation measurement (Du et al., 2020b), with daily average values of T_a ranging from -16 °C to -10.5 °C between sites, and T_{mrt} measurements ranging between -7 °C and 52 °C, similar to the range obtained from Guelph on February 3, 2021 (-11.6 °C to 46.8 °C). A drawback to using T_{mrt} to assess wintertime thermal exposure derives from the high relative importance of wind speed (v). v is an important component of *UTCI* and cold exposure more generally. For example, metrics such as the wind chill temperature rely only on the combination of T_a and v (Osczevski & Bluestein, 2005). Because T_{mrt} only captures pedestrian radiation exposure, other metrics should be considered in wintertime thermal comfort research. Limitations in the temporal sampling of v in this study may have caused some lack of representativeness in resulting *UTCI* values, with our short measurement periods at each site probably unable to account for the mean impacts of wind fluctuations.

Studies during summer heat wave periods have shown how the use of high-albedo materials decreases air and surface temperature but additionally increases the reflection of shortwave radiation toward the pedestrian, elevating heat exposure (Erell et al., 2014; Lee & Mayer, 2018; Middel et al., 2020; Schneider et al., 2023). In winter, snow surfaces can mimic the reflective effects of high-albedo materials, depending on the age and cleanliness of the snow. Thus, snow surfaces may be beneficial in the reduction of daytime pedestrian cold exposure. The current measurements in February demonstrate that near the daytime peak of solar radiation (1200 EST), four of the top five most comfortable locations, as classified with *UTCI,* were over snow, with the final location being over a light concrete surface. After sunset, sites over snow became more uncomfortable than other sites on average, dependent on Ψ_{sky} and proximity to building cover, largely because of the low nighttime surface temperature of snow relative to different surfaces with higher thermal admittance.

The sensitivity of *PET* and *UTCI* to their constituent meteorological variables for the June and February measurement days revealed that both indices were more sensitive to T_a than to T_{mrt} (Supplementary Figs. 9 and 10; Aiello, 2022), consistent with the hot, dry conditions examined by Middel and Krayenhoff (2019). However, in June, T_{mrt} effectively captured the large spatial variation of pedestrian thermal exposure, unlike T_a. Moreover, *PET* and *UTCI* were not used to analyze warm weather days because T_{mrt} could explain most of the spatial

variation in each index ($R^2 = 0.953$; Aiello, 2022). For analysis of winter (e.g., February) measurements, *UTCI* was preferred over *PET* due to its dynamic clothing model, and it was used instead of T_{mrt} because it captures the impacts of other meteorological variables, especially wind. *UTCI* was deemed a strong predictor of cold weather thermal sensation, outperforming *PET* and Standard Effective Temperature (*SET*), modelled during winter in Harbin, China (Chen et al., 2020). There are few, if any, cold weather studies that have gathered detailed radiative flux measurements to determine pedestrian thermal comfort using *UTCI*, and future research should expand upon this gap to gather accurate thermal comfort measurements for cities that experience cold winters.

This study investigated microscale controls on T_{mrt} during warm and cold weather conditions by evaluating directional shortwave and longwave radiation fluxes, weighted to represent the radiative exchanges experienced by a pedestrian. Summertime radiation flux results were consistent with studies in Tempe, Arizona (Middel & Krayenhoff, 2019) and Freiburg, Germany (Ali-Toudert & Mayer, 2007; Lee et al., 2014): L_{lat} provided the majority of the radiative heat exposure on a pedestrian, with K_i determining where maximum heat exposure occurred, depending primarily on shade during daytime. Cold weather relationships were consistent with a study in Harbin, China (Du et al., 2020b), with K_i having a proportionally higher impact on mitigating cold exposure since cold surfaces emitted less longwave.

For the clear sky cases examined here, shade was the most important factor determining daytime radiative exposure during all seasons, with surface ground cover having a secondary effect, particularly during summer (Figs. 3 and 4), consistent with the findings of Lindberg et al. (2016) for London, England. Influences on T_{mrt}, including sky, impervious and pervious view factors, were consistent with Middel and Krayenhoff (2019) in summer and Du et al. (2020b) in winter. In the current measurements, the increase in longwave radiation incident on a pedestrian as a function of the increased impervious surface view factor was more evident in the summer than during winter. June measurements of T_{sfc} over grass were up to 10 °C cooler than over impervious surfaces, independent of sunlight hours received per site, affecting T_{mrt} as a result. This relationship was also present during February, but replacing pervious grass with cold snow surfaces resulted in a unique outcome during daylight hours: decreased longwave radiation from the colder snow was more than balanced by increases in reflected shortwave radiation. When not sunlit, snow can become much colder than impervious surfaces due to its insulating properties. This effect can be particularly strong with sufficient sky exposure and, therefore, reduced incoming longwave radiation.

Impacts of surface structure and cover on T_{mrt} are quantifiable from the results. At 1500 EDT on June 6, a Ψ_{sky} reduction of 0.1 decreased T_{mrt} by 3.6 °C on average, driven by the lower magnitudes of shortwave and longwave radiation at sites with smaller Ψ_{sky} ($R^2 = 0.63$). When unshaded, T_{mrt} over grass was 4 °C lower than that over asphalt and 8 °C lower than that over concrete in part because the T_{sfc} of grass was 14 °C and 21 °C lower than the T_{sfc} of concrete and asphalt, respectively. At night (2200 EDT), the combination of sky view factor Ψ_{sky} (cooling) and lateral impervious view factor I_{360} (warming) best explained T_{mrt} variation ($R^2 = 0.85$).

On Feb. 3, increasing access to the sun (i.e., a 0.1 increase in Ψ_{sky}) increased T_{mrt} and *UTCI* by 6.1 °C and 2.3 °C, respectively, for the locations and times studied here ($R^2 = 0.34$ in each model). At night (18:30 EST), this effect was opposite and smaller, lowering T_{mrt} and *UTCI* by 1.1 °C and 0.63 °C, respectively, per 0.1 increase in Ψ_{sky}. Combining Ψ_{sky} and Sn_{360} explained most variation in T_{mrt} ($R^2 = 0.72$) at night, with higher pedestrian exposure to sky and snow yielding lower T_{mrt}.

It is worth noting that pedestrians can choose different locations within the built environment to reduce thermal stress, for example by walking on the shaded side of the street during hot afternoon conditions (i.e., thermal adaptive behavior). However, our objective here is to examine the pedestrian exposure that would occur in a variety of locations with differing local ground cover and built/tree geometry, in order to better understand the physics of what makes for low compared to high thermal stress conditions. This knowledge can then be applied to design streets and urban spaces that have a greater spatial coverage of thermally comfortable spaces.

There are a number of helpful extensions to the research undertaken herein. In each season of data collection, combined lateral tree and grass cover (P_{360}) did not effectively explain the variation in T_{mrt} or *UTCI*, highlighting the need for a greater diversity of sites containing trees, grass, and green walls to explain their impact on thermal exposure. The use of separate vertical (e.g., tree) and horizontal (e.g., grass) pervious view factors would assist. Similarly, impervious view factors should be separated into vertical and horizontal components to disentangle their radiative (e.g., building shade) and heat storage (e.g., warm asphalt) impacts. Future research into cold weather pedestrian thermal exposure and comfort using *UTCI* should focus on alternative methods to collect wind speed data to better represent the hourly average wind experienced at a site. Intra-hourly wind speed measurements would capture the variation introduced by gusting conditions, resulting in a better characterization of wind speeds at each site.

Finally, the six-directional method permits evaluation of the directional loading of shortwave and longwave radiation on pedestrians, thus enabling refined assessment of the impacts of different surface structures, covers, and materials, as well as their spatial configuration, on pedestrian thermal exposure. This additional radiative flux information can be used to evaluate advanced models of pedestrian thermal exposure that capture detailed spatio-temporal variation of surface temperature and directional longwave (and shortwave) loading on pedestrians (e.g., TUF-Pedestrian; Lachapelle et al. 2022). Recently, Jiang et al. (2023) used the dataset presented here to further evaluate TUF-Pedestrian.

5. Summary and conclusions

Six-directional shortwave and longwave radiation, air temperature, humidity, and wind speed were collected on September 15, 2020, November 28, 2020, February 1st and 3rd, 2021, and June 6, 2021, in Guelph, Canada, using a mobile human-biometeorological weather station (*MaRTy*). Measurements were gathered during hourly transects at 23 unique locations (21 in February) at the University of Guelph main campus, with shade at each location provided by buildings and trees and surface ground covers consisting of asphalt, concrete, brick, grass, or snow in winter. It was one of the hottest June 6 days on record, with peak measured air temperature (T_a) of 31.9 °C. On February 3, measured air temperature (T_a) dropped as low as -3.3 °C.

5.1. Summary of findings

5.1.1. June 6, 2021 (extreme heatt day)

At 1500 EDT, the thermal index *UTCI* reached a spatial maximum of 40.2 °C at site 19 (new concrete) in direct sunlight. At this time, the most thermally comfortable locations exhibited a low sky view factor (Ψ_{sky}) and were shaded by trees or buildings, with UTCI 6 °C-10 °C lower than the spatial maximum. At all times of day, longwave fluxes contributed more to overall T_{mrt} than shortwave fluxes, providing a baseline level of thermal exposure. Shortwave radiation fluxes provided most of the spatio-temporal variation of T_{mrt}, with sites in direct sunlight experiencing the highest levels of outdoor thermal exposure. During the daytime, T_{mrt} varied by as much as 41.3 °C between fully shaded and unshaded sites. Results indicate that daytime pedestrian T_{mrt} is reduced during hot, humid weather in Guelph with increased shade and secondarily by replacing impervious surface cover with pervious materials. At night, increased sky view factor and decreased lateral impervious view factor were similarly predictive of T_{mrt} reduction.

5.1.2. February 3, 2021 (cold day with snow cover)

During daytime, the spatial variation of *UTCI* reached 31 °C, ranging

from -13 °C (shaded) to 18 °C (unshaded). At night, open sites became coldest, with *UTCI* ranging from -12.7 °C to -1.8 °C. Similar to June, *UTCI* was more sensitive to changes in T_a than T_{mrt} per degree Celsius (Aiello, 2022); however, T_{mrt} better captured the spatio-temporal variation of thermal exposure experienced between sites with high and low Ψ_{sky}. After sunset (18:30 EST), the thermal index *UTCI* averaged -6.5 °C across all sites and reached a minimum of -12.7 °C at site 21 (asphalt under open skies).

During the day, shortwave radiation was the largest component of both T_{mrt} and *UTCI* at partially or fully unshaded sites. Shortwave radiation proportionally had a much stronger impact on outdoor thermal exposure than in June, since colder surface temperatures meant longwave radiation was smaller in magnitude. Moreover, the presence of snow during daytime increased shortwave radiation fluxes (as evidenced by greater values of K_{up} over snow) by means of reflection, alleviating cold exposure. The thermal drawback related to snow occurred after sunset, when sites with more snow cover had the coldest surface temperatures, by up to 8 °C relative to sites surrounded by impervious surface covers. The relatively low snow surface temperature resulted in smaller magnitudes of upwelling longwave radiation and lower average T_{mrt} and *UTCI* (8.7 °C and 3.3 °C lower, respectively) at these sites.

5.1.3. Year-round pedestrian thermal comfort

In June, recommendations involve adding shade and replacing impervious surface cover with pervious cover to alleviate heat exposure. In February, shade amplifies the impacts of daytime cold exposure, creating thermally uncomfortable pedestrian environments. Daytime cold exposure was alleviated with access to open, sunlit areas in winter. Deciduous tree cover could present a dual benefit in alleviating heat and cold exposure in each season by providing canopy shade in summer and allowing sunlight to reach pedestrian areas in winter when leaves drop in the autumn months. Alternatively, artificial shade in summer could provide benefits similar to trees without watering, leaf collection, and maintenance, provided it is removed in winter to allow greater solar irradiance at the pedestrian level. In winter, snow increased reflected shortwave radiation, improving pedestrian thermal comfort, suggesting that leaving fresh snow adjacent to pedestrian areas may be helpful (albeit not so after sunset).

CRediT authorship contribution statement

Timothy Aiello: Writing – original draft, Visualization, Software, Methodology, Investigation, Formal analysis, Data curation. **E. Scott Krayenhoff:** Writing – review & editing, Supervision, Project administration, Methodology, Investigation, Funding acquisition. **Ariane Middel:** Writing – review & editing, Supervision, Methodology, Conceptualization. **Jon Warland:** Writing – review & editing, Supervision, Funding acquisition.

Declaration of competing interest

The authors declare the following financial interests/personal relationships which may be considered as potential competing interests:

E. Scott Krayenhoff reports financial support was provided by Natural Sciences and Engineering Research Council of Canada. If there are other authors, they declare that they have no known competing financial interests or personal relationships that could have appeared to influence the work reported in this paper.

Acknowledgements

Thanks are due to Jacob Lachapelle, Nicole Menheere, Eric Ken, Sophia Teng, and Sarah Duke for assisting with *MaRTy* data collection. Tim Jiang assisted with the datalogger code, James Voogt loaned the fisheye camera, and Mieke Boecker assisted with editing the manuscript. This research was funded by an NSERC Discovery Grant to ESK, and by University of Guelph funds provided to ESK and JW. AM acknowledges support from NSF CAREER grant #CMMI-1942805.

Supplementary materials

Supplementary material associated with this article can be found, in the online version, at doi:10.1016/j.scs.2024.106019.

Data availability

MaRTy measurement data underlying the analysis presented in this article is available at: https://borealisdata.ca/dataset.xhtml?persistentId=doi:10.5683/SP3/YY1GCU.

References

Ahrens, D., & Henson, R. (2013). *Meteorology today: an introduction to weather, climate, and the environment* (11th ed.). Boston, MA: Cengage Learning.

Aiello, T. (2022). *MSc dissertation*. University of Guelph.

Ali-Toudert, F., Djenane, M., & Bensalem, R. (2005). Outdoor thermal comfort in the old desert city of Beni-Isguen, Algeria. *Climate Research, 28*, 243–256.

Ali-Toudert, F., & Mayer, H. (2007). Thermal comfort in an east-west oriented street canyon in Freiburg (Germany) under hot summer conditions. *Theoretical and Applied Climatology, 87*, 223–237. https://doi.org/10.1007/s00704-005-0194-4

Analitis, A., Katsouyanni, K., Biggeri, A., Baccini, M., Forsberg, B., Bisanti, L., Kirchmayer, U., Ballester, F., Cadum, E., Goodman, P.G., Hojs, A., Sunyer, J., Tiittanen, P., Michelozzi, P., 2008. Effects of cold weather on mortality: Results from 15 european cities within the PHEWE Project 168, 1397–1408. https://doi.org/10.1093/aje/kwn266.

Argueso, D., Evans, J. P., Fita, L., & Bormann, K. J. (2014). Temperature response to future urbanization and climate change. *Climate Dynamics, 42*, 2183+.

Bröde, P., Fiala, D., Błażejczyk, K., Holmér, I., Jendritzky, G., Kampmann, B., Tinz, B., & Havenith, G. (2012). Deriving the operational procedure for the Universal Thermal Climate Index (UTCI). *International Journal of Biometeorology, 56*, 481–494. https://doi.org/10.1007/s00484-011-0454-1

Chen, X., Gao, L., Xue, P., Du, J., & Liu, J. (2020). Investigation of outdoor thermal sensation and comfort evaluation methods in severe cold area. *Science of the Total Environment, 749*, Article 141520. https://doi.org/10.1016/j.scitotenv.2020.141520

Chen, H., Wang, J., Li, Q., Yagouti, A., Lavigne, E., Foty, R., Burnett, R. T., Villeneuve, P. J., Cakmak, S., & Copes, R. (2016). Assessment of the effect of cold and hot temperatures on mortality in Ontario, Canada: a population-based study. *C. Open, 4*, E48–E58. https://doi.org/10.9778/cmajo.20150111

Crisci, A., Morabito, M., 2016. rBiometeo: Biometeorological Functions in R [WWW Document]. URL https://github.com/alfcrisci/rBiometeo.

Di Matteo, L. (2005). The macro determinants of health expenditure in the United States and Canada: assessing the impact of income, age distribution and time. *Health Policy (New. York), 71*, 23–42. https://doi.org/10.1016/j.healthpol.2004.05.007

Du, J., Liu, L., Chen, X., & Liu, J. (2020a). Field assessment of neighboring building and tree shading effects on the 3D radiant environment and human thermal comfort in summer within urban settlements in Northeast China. *Advances in Meteorology, 2020*, Article 8843676. https://doi.org/10.1155/2020/8843676

Du, J., Sun, C., Xiao, Q., Chen, X., & Liu, J. (2020b). Field assessment of winter outdoor 3-D radiant environment and its impact on thermal comfort in a severely cold region. *Science of the Total Environment, 709*, Article 136175. https://doi.org/10.1016/j.scitotenv.2019.136175

Erell, E., Pearlmutter, D., Boneh, D., & Kutiel, P. B. (2014). Effect of high-albedo materials on pedestrian heat stress in urban street canyons. *Urban Clim., 10*, 367–386. https://doi.org/10.1016/j.uclim.2013.10.005

Givoni, B., Noguchi, M., Saaroni, H., Pochter, O., Yaacov, Y., Feller, N., & Becker, S. (2003). Outdoor comfort research issues. *Energy and Buildings, 35*, 77–86. https://doi.org/10.1016/S0378-7788(02)00082-8

Gosling, S. N., Lowe, J. A., McGregor, G. R., Pelling, M., & Malamud, B. D. (2009). Associations between elevated atmospheric temperature and human mortality: a critical review of the literature. *Climatic Change, 92*, 299–341. https://doi.org/10.1007/s10584-008-9441-x

Government of Canada, 2019. Population Projections for Canada (2018 to 2068), Provinces and Territories (2018 to 2043) [WWW Document]. URL https://www150.statcan.gc.ca/n1/pub/91-520-x/91-520-x2019001-eng.htm.

Government of Canada, 2020. Canadian Climate Normals 1981-2010 Station Data.

Guzman-Echavarria, G., Middel, A., & Vanos, J. (2023). Beyond heat exposure—new methods to quantify and link personal heat exposure, stress, and strain in diverse populations and climates: The journal temperature toolbox. *Temperature, 10*(3), 358–378.

Häb, K., Ruddell, B. L., & Middel, A. (2015). Sensor lag correction for mobile urban microclimate measurements. *Urban Clim., 14*, 622–635. https://doi.org/10.1016/j.uclim.2015.10.003

Havenith, G., Fiala, D., Błazejczyk, K., Richards, M., Bröde, P., Holmér, I., Rintamaki, H., Benshabat, Y., & Jendritzky, G. (2012). The UTCI-clothing model. *International Journal of Biometeorology, 56*, 461–470. https://doi.org/10.1007/s00484-011-0451-4

Holst, J., & Mayer, H. (2011). Impacts of street design parameters on human-biometeorological variables. *Meteorol. Zeitschrift, 20*, 541–552. https://doi.org/10.1127/0941-2948/2011/0254

Hondula, D. M., Balling, R. C., Andrade, R., Krayenhoff, E. S., Middel, A., Urban, A., Georgescu, M., & Sailor, D. J. (2017). Biometeorology for cities. *International Journal of Biometeorology, 61*, 59–69. https://doi.org/10.1007/s00484-017-1412-3

Hondula, D. M., Balling, R. C., Vanos, J. K., & Georgescu, M. (2015). Rising temperatures, human health, and the role of adaptation. *Current Climate Change Reports, 1*, 144–154. https://doi.org/10.1007/s40641-015-0016-4

Höppe, P. (1992). Ein neues verfahren zur bestimmung der mittleren strahlungstemperatur im Freien. *Wetter und Leb, 44*, 147–151.

Höppe, P. (1999). The physiological equivalent temperature - a universal index for the biometeorological assessment of the thermal environment. *International Journal of Biometeorology, 43*, 71–75.

IPCC, 2014. Climate Change 2014: Synthesis Report. Contribution of Working Groups I, II and III to the Fifth Assessment Report of the Intergovernmental Panel on Climate Change.

IPCC, 2021. Summary for Policymakers. Climate Change 2021: The Physical Science Basis. 41.

ISO, 1998. ISO 7726, Ergonomics of the Thermal Environment, Instruments for Measuring Physical Quantities. htt ps://doi.org/ISO7726:1998(E).

Jendritzky, G., de Dear, R., & Havenith, G. (2012). UTCI-Why another thermal index? *International Journal of Biometeorology, 56*, 421–428. https://doi.org/10.1007/s00484-011-0513-7

Jiang, T., Krayenhoff, E. S., Voogt, J. A., Warland, J., Demuzere, M., & Moede, C. (2023). Dynamically downscaled projection of urban outdoor thermal stress and indoor space cooling during future extreme heat. *Urban Climate, 51*, Article 101648t()])"_ $^!"local-name(child::*[last()])">.

Kántor, N., Chen, L., & Gál, C. V (2018). Human-biometeorological significance of shading in urban public spaces—Summertime measurements in Pécs, Hungary. *Landscape and Urban Planning, 170*, 241–255. https://doi.org/10.1016/j.landurbplan.2017.09.030

Kántor, N., Kovács, A., & Takács, Á. (2016). Small-scale human-biometeorological impacts of shading by a large tree. *Open Geosci, 8*, 231–245. https://doi.org/10.1515/geo-2016-0021

Krayenhoff, E. S., Moustaoui, M., Broadbent, A. M., Gupta, V., & Georgescu, M. (2018). Diurnal interaction between urban expansion, climate change and adaptation in US cities. *Nature Climate Change, 8*, 1097–1103. https://doi.org/10.1038/s41558-018-0320-9

Lachapelle, J. A., Krayenhoff, E. S., Middel, A., Meltzer, S., Broadbent, A. M., & Georgescu, M. (2022). A microscale three-dimensional model of urban outdoor thermal exposure (TUF-Pedestrian). *International Journal of Biometeorology, 66*(4), 833–848.

Lai, A., Kwok, Y. T., Maing, M., & Ng, E. (2018). Regression modelling of radiant fluxes on different view factors under shading in a densely built environment. *Architectural Science Review, 61*, 15–28. https://doi.org/10.1080/00038628.2017.1409614

Lai, D., Zhou, C., Huang, J., Jiang, Y., Long, Z., & Chen, Q. (2014). Outdoor space quality: A field study in an urban residential community in central China. *Energy and Buildings, 68*, 713–720. https://doi.org/10.1016/j.enbuild.2013.02.051

Lee, H., & Mayer, H. (2018). Thermal comfort of pedestrians in an urban street canyon is affected by increasing albedo of building walls. *International Journal of Biometeorology, 62*, 1199–1209. https://doi.org/10.1007/s00484-018-1523-5

Lee, H., Mayer, H., & Schindler, D. (2014). Importance of 3-D radiant flux densities for outdoor human thermal comfort on clear-sky summer days in Freiburg, Southwest Germany. *Meteorol. Zeitschrift, 23*, 315–330. https://doi.org/10.1127/0941-2948/2014/0536

Lindberg, F., Holmer, B., & Thorsson, S. (2008). SOLWEIG 1.0 - Modelling spatial variations of 3D radiant fluxes and mean radiant temperature in complex urban settings. *International Journal of Biometeorology, 52*, 697–713. https://doi.org/10.1007/s00484-008-0162-7

Lindberg, F., Onomura, S., & Grimmond, C. S. B. (2016). Influence of ground surface characteristics on the mean radiant temperature in urban areas. *International Journal of Biometeorology*, 1439–1452. https://doi.org/10.1007/s00484-016-1135-x

Matzarakis, A., Rutz, F., & Mayer, H. (2010). Modelling radiation fluxes in simple and complex environments: Basics of the RayMan model. *International Journal of Biometeorology, 54*, 131–139. https://doi.org/10.1007/s00484-009-0261-0

Matzarakis, A., Rutz, F., & Mayer, H. (2007). Modelling radiation fluxes in simple and complex environments - Application of the RayMan model. *International Journal of Biometeorology, 51*, 323–334. https://doi.org/10.1007/s00484-006-0061-8

Mayer, H., Holst, J., Dostal, P., Imbery, F., & Schindler, D. (2008). Human thermal comfort in summer within an urban street canyon in Central Europe. *Meteorol Zeitschrift, 17*, 241–250. https://doi.org/10.1127/0941-2948/2008/0285

McGeehin, M. A., & Mirabelli, M. (2001). The potential impacts of climate variability and change on temperature-related morbidity and mortality in the United States. *Environmental Health Perspectives, 109*, 185–189. https://doi.org/10.2307/3435008

Middel, A., AlKhaled, S., Schneider, F. A., Hagen, B., & Coseo, P. (2021). 50 grades of shade. *Bulletin of the American Meteorological Society, 102*(9), E1805–E1820.

Middel, A., Huff, M., Krayenhoff, E. S., Udupa, A., & Schneider, F. A. (2023). PanoMRT: Panoramic infrared thermography to model human thermal exposure and comfort. *Science of The Total Environment, 859*, Article 160301.

Middel, A., & Krayenhoff, E. S. (2019). Micrometeorological determinants of pedestrian thermal exposure during record-breaking heat in Tempe, Arizona: Introducing the MaRTy observational platform. *Science of the Total Environment, 687*, 137–151. https://doi.org/10.1016/j.scitotenv.2019.06.085

Middel, A., Turner, V. K., Schneider, F. A., Zhang, Y., & Stiller, M. (2020). Solar reflective pavements-A policy panacea to heat mitigation? *Environmental Research Letters, 15*, 64016. https://doi.org/10.1088/1748-9326/ab87d4

Oke, T., Mills, G., Christen, A., & Voogt, J. (2017). *Urban climates*. Cambridge: Cambridge University Press.

Osczevski, R., & Bluestein, M. (2005). The new wind chill equivalent temperature chart. *Bulletin of the American Meteorological Society, 86*, 1453–1458.

Piselli, C., Castaldo, V. L., Pigliautile, I., Pisello, A. L., & Cotana, F. (2018). Outdoor comfort conditions in urban areas: On citizens' perspective about microclimate mitigation of urban transit areas. *Sustainable Cities and Society, 39*, 16–36.

Schneider, F. A., Ortiz, J. C., Vanos, J. K., Sailor, D. J., & Middel, A. (2023). Evidence-based guidance on reflective pavement for urban heat mitigation in Arizona. *Nature Communications, 14*(1), 1467.

Statistics Canada, 2021. Canada's population estimates: Subprovincial areas, July 1, 2014 1–6.

Stewart, I. D., Krayenhoff, E. S., Voogt, J. A., Lachapelle, J. A., Allen, M. A., & Broadbent, A. M. (2021). Time evolution of the surface urban heat island. *Earth's Future, 9*(10), Article e2021EF002178.

Thorsson, S., Lindberg, F., Eliasson, I., Holmer, B., 2007. Different methods for estimating the mean radiant temperature in an outdoor urban setting 1993, 1983–1993. https://doi.org/10.1002/joc.

United Nations, 2019. World Urbanization Prospects: The 2018 Revision, Demographic Research. New York.

University of Guelph, 2013. About the University [WWW Document]. URL https://web.archive.org/web/20130527110037/http://www.uoguelph.ca/info/factsfigures/.

Vanos, J. K., Rykaczewski, K., Middel, A., Vecellio, D. J., Brown, R. D., & Gillespie, T. J. (2021). Improved methods for estimating mean radiant temperature in hot and sunny outdoor settings. *International Journal of Biometeorology, 65*(6), 967–983.

VDI, 1998. Methods for the human biometeorological evaluation of climate and air quality for urban and regional planning at regional level Part I: Climate.

Wouters, H., De Ridder, K., Poelmans, L., Willems, P., Brouwers, J., Hosseinzadehtalaei, P., Tabari, H., Vanden Broucke, S., van Lipzig, N. P. M., & Demuzere, M. (2017). Heat stress increase under climate change twice as large in cities as in rural areas: A study for a densely populated midlatitude maritime region. *Geophysical Research Letters, 44*, 8997–9007. https://doi.org/10.1002/2017GL074889

Xiong, K., & He, B. J. (2022). Wintertime outdoor thermal sensations and comfort in cold-humid environments of Chongqing China. *Sustainable Cities and Society, 87*, Article 104203.

Xu, M., Hong, B., Mi, J., & Yan, S. (2018). Outdoor thermal comfort in an urban park during winter in cold regions of China. *Sustainable cities and society, 43*, 208–220.

Yao, J., Yang, F., Zhuang, Z., Shao, Y., & Yuan, P. F. (2018). The effect of personal and microclimatic variables on outdoor thermal comfort: A field study in a cold season in Lujiazui CBD, Shanghai. *Sustainable Cities and Society, 39*, 181–188.